

**KU LEUVEN**

 **FACULTY OF  
ENGINEERING SCIENCE**

# Reliability analysis of a high pressure hydrogen tank for Fuel Cell Electric Vehicles

Iron Degryse

Thesis submitted for the degree of  
Master of Science in Mechanical  
Engineering

**Thesis supervisors:**  
Prof. dr. ir. Dirk Vandepitte  
Prof. dr. ir. David Moens

Academic year 2021 – 2022

**Master of Science in Mechanical Engineering**

# Reliability analysis of a high pressure hydrogen tank for Fuel Cell Electric Vehicles

Iron Degryse

Thesis submitted for the degree of  
Master of Science in Mechanical  
Engineering

**Thesis supervisors:**

Prof. dr. ir. Dirk Vandepitte  
Prof. dr. ir. David Moens

**Assessors:**

Prof. dr. ir. Johan Steelant  
Dr. ir. Antonio Cutolo

**Mentors:**

Ir. Ben Van Bavel  
Ir. Rafael Alexandre Mota dos Santos

© Copyright KU Leuven

Without written permission of the thesis supervisors and the author it is forbidden to reproduce or adapt in any form or by any means any part of this publication. Requests for obtaining the right to reproduce or utilize parts of this publication should be addressed to Faculteit Ingenieurswetenschappen, Kasteelpark Arenberg 1 bus 2200, B-3001 Heverlee, +32-16-321350.

A written permission of the thesis supervisors is also required to use the methods, products, schematics and programmes described in this work for industrial or commercial use, and for submitting this publication in scientific contests.



# Preface

With this thesis, there comes an end to my educational path and academic career. After graduating from high school, the choice for engineering sciences wasn't a hard one. I always liked mathematics and physics - especially the course on mechanics we got in the sixth year. It is somehow funny to see that five years later, I (hopefully) will graduate as a mechanical engineer. Apparently, sometimes the future can be predicted.

If everything goes to plan, a new part of my life will start in August. I will work at ArcelorMittal Ghent as quality specialist for the automotive sector. I look very much forward to this new experience. Although I liked my time at the universities of Kortrijk and Leuven, I feel like my academic appetite has been satisfied. What I will miss are the many inspiring people I met the last years, in- and outside the university. I hope to stay in contact with many of them.

Regarding the thesis itself, I am very grateful that I could gain practical experience with finite element modelling in the field of structural engineering. The thesis has been a combination of my two favourite courses of the master program: 'Numerical Modelling in Mechanical Engineering' and 'Theory of Elasticity and Plasticity'. I really feel like I became a better engineer during the course of the thesis. Starting from a theoretical basis, I progressively learned how to practically implement features that are already pretty advanced (composite modelling, contact mechanisms, failure determination, ...).

Off course, this would have been impossible without the help of the staff. In the first place, I owe a lot to ir. Ben van Bavel and ir. Rafael Alexandre Mota dos Santos (my daily supervisors). They were very engaged and were always willing to help me with practical issues or phenomena I didn't understand. I also want to thank my promoters, prof. dr. ir. Dirk Vandepitte and prof. dr. ir. David Moens. With their experience, they were able to point to key matters and guided me in the right direction. Lastly, I want to thank my parents and my friends. I was always welcome to talk about the thesis and pieces of motivation were given when I needed them.

# Contents

<b>Contents</b>	<b>ii</b>
<b>Abstract</b>	<b>iv</b>
Samenvatting . . . . .	v
<b>1 Problem formulation</b>	<b>1</b>
1.1 Usage case for fibre composites . . . . .	1
1.2 Fuel cell electric vehicles . . . . .	2
1.3 Composite pressure vessels . . . . .	3
1.3.1 Morphology . . . . .	3
1.3.2 Production . . . . .	5
1.4 Ring test: assessing failure . . . . .	6
1.5 Conclusions . . . . .	8
<b>2 Nominal modelling</b>	<b>9</b>
2.1 Nominal situation . . . . .	9
2.2 Classical laminate theory . . . . .	11
2.3 Elastic composite, subjected to hydraulic pressure (FE) . . . . .	14
2.3.1 Development of the model . . . . .	14
2.3.2 Solution of the model . . . . .	15
2.4 Imitation of the ring test mechanisms (FE) . . . . .	22
2.4.1 Development of the model . . . . .	22
2.4.2 Solution of the model . . . . .	25
2.4.3 Failure determination . . . . .	31
2.4.4 Convergence study . . . . .	33
2.5 Conclusions . . . . .	37
<b>3 Sensitivity analysis</b>	<b>39</b>
3.1 Local sensitivity analysis . . . . .	39
3.2 Global sensitivity analysis . . . . .	47
3.2.1 Determination of the Sobol' indices . . . . .	47
3.2.2 Histogram of the burst pressure . . . . .	52
3.3 Conclusions . . . . .	54
<b>4 Conclusions</b>	<b>55</b>
4.1 Results . . . . .	55
4.2 Further work . . . . .	57

<b>5 Appendices</b>	<b>58</b>
5.1 Code for CLT-calculations (Van Bavel) . . . . .	58
5.2 Results of the test campaign . . . . .	61
<b>Bibliography</b>	<b>62</b>

# Abstract

Minimizing the ecological footprint of human activity, while maintaining a comfortable and affordable way of living is probably one of the biggest challenges in the 21st century. One of the fields where a lot of innovation is going on at the moment in this context is the automobile industry, where alternatives are sought for fossil fuel cars. An important example of these alternatives are fuel cell electric vehicles. They combine low emissions with a usage pattern that is comparable to those of fossil fuel cars. They seem especially interesting for heavy duty transport.

While the physical concept seems attractive, there still remains a lot of technological development and optimization to be done. This thesis focuses on a vital part of the drive system in a fuel cell electric vehicle: the pressure vessel where the hydrogen (and thus the energy) is stored. It is the most heavy part of the drive system, and thus increases the power demand of the vehicle significantly (1). As a solution to limit the weight of the structure, alternative materials are sought to replace steel. One material group with a very high specific strength and stiffness are the fibre composites.

While they technically outperform, there remain some problems. Fibre composites are less mature and their mechanical behaviour is inherently more difficult to model. This leaves companies nowadays with a choice between two unattractive options: perform big time consuming and expensive experiment campaigns or use a very big safety factor. The industry standard for the safety factors of composite pressure vessels is now around 2.25 (2).

This thesis deals with an alternative approach to assess the structural reliability of a composite pressure vessel, a so-called ring test. Here, the hydraulic pressure of the hydrogen is imitated by a radial contact mechanism and applied to a ring specimen. In this way, a lot of testing material can be saved. The ambition is to develop a template in which the ring test is combined with an extensive virtual test campaign (finite element model). This combination could limit the cost of the test campaign, while maintaining a reasonably low safety factor.

In this thesis, models for the ring test are developed and verified. Relations between the design variables, other givens and the burst pressure are studied. In this way, an objective and numerical assessment of the (dis)advantages of the ring test is made.



## Samenvatting

Het minimaliseren van de menselijke, ecologische voetafdruk en het behouden van een comfortabele en betaalbare levenswijze is waarschijnlijk één van de grootste uitdagingen van de 21e eeuw. Één van de terreinen waar op dit moment veel innovatie plaatsvindt in deze context is de auto-industrie, waar wordt gezocht naar alternatieven voor auto's op fossiele brandstof. Een belangrijk voorbeeld van deze alternatieven zijn brandstofcel-elektrische voertuigen. Ze combineren een lage uitstoot met een gebruikspatroon dat vergelijkbaar is met dat van auto's op fossiele brandstof. Vooral voor zwaar transport lijken ze interessant.

Hoewel het fysieke concept aantrekkelijk lijkt, moet er nog veel technologische ontwikkeling en optimalisatie plaatsvinden. Dit proefschrift richt zich op een essentieel onderdeel van het aandrijfsysteem in een brandstofcel elektrisch voertuig: het drukvat waar de waterstof (en dus de energie) wordt opgeslagen. Het is het zwaarste onderdeel van het aandrijfsysteem en verhoogt dus de vermogensbehoefte van het voertuig aanzienlijk (1). Als oplossing om het gewicht van de constructie te beperken, wordt gezocht naar alternatieve materialen ter vervanging van staal. Een materiaalgroep met een zeer hoge specifieke sterkte en stijfheid zijn de vezelcomposieten.

Hoewel ze technisch beter presteren, blijven er enkele problemen. Vezelcomposieten zijn minder matuur en hun mechanisch gedrag is inherent moeilijker te modelleren. Hierdoor hebben bedrijven tegenwoordig de keuze tussen twee onaantrekkelijke opties: grote tijdrovende en dure experimentcampagnes uitvoeren of een zeer grote veiligheidsfactor gebruiken. De industriestandaard voor de veiligheidsfactoren van composiet drukvaten ligt nu rond de 2,25 (2).

Dit proefschrift behandelt een alternatieve benadering om de structurele betrouwbaarheid van een composiet drukvat te beoordelen, een zogenaamde ringtest. Hier wordt de hydraulische druk van de waterstof nagebootst door een radiaal contactmechanisme naar een ringmonster toe. Op deze manier kan veel testmateriaal worden bespaard. De ambitie is om een template te ontwikkelen waarin de ringtest wordt gecombineerd met een uitgebreide virtuele testcampagne (= eindige elementenmodel). Deze combinatie zou de kosten van de testcampagne kunnen beperken, terwijl de veiligheidsfactor redelijk laag blijft.

In dit proefschrift worden modellen voor de ringtest ontwikkeld en geverifieerd. Relaties tussen de ontwerpvariabelen, andere gegevens en de barstdruk worden bestudeerd. Op deze manier wordt een objectieve en cijfermatige inschatting gemaakt van de (na)delen van de ring test.



# Chapter 1

## Problem formulation

In this section, the goal of this thesis will be situated and formulated. Firstly, the usage case for fibre composites in structural design will be motivated, including its benefits and challenges. Secondly, the more specific context of fuel cell electric vehicles will be presented. Thirdly, the morphology and production of composite pressure vessels will be dealt with. Finally, the possibility of a ring test will be elaborated to assess the burst pressure and failure mode of the composite pressure vessel.

### 1.1 Usage case for fibre composites

Metals are the standard industry material group when high loads have to be supported, due to their high strength and ditto stiffness. However, they have a big disadvantage: they are heavy. This is especially disadvantageous in transport applications, such as aviation and automotive industry.

Therefore, in these industries the usage of unidirectional carbon-fiber-reinforced polymers (CFRP) has taken a big rise. An example of an application where the carbon fibre components have become omnipresent is the Boeing 787, which consists of around 50 percent of composite material. Most of that composite material is either carbon fiber laminate or carbon fiber sandwich (3).

The specific strength and specific modulus of these composites is a lot higher in the fibre direction than those of commonly used metals such as carbon steel, aluminium and titanium (see Fig. 1.1, (4)). This usage, however, poses a challenge to engineers designing these structural elements. Indeed, on the macroscale CFRPs show orthotropic behaviour, while on the microscale there is a lot of spatial variation due to manufacturing imperfections. These features influence the mechanical behaviour and therefore should be included in a structural analysis. A complete test campaign is time and cost-intensive, so big safety factors are used instead of more extensive testing (2). This currently stops the material from fulfilling its potential, both in application range and energy savings.

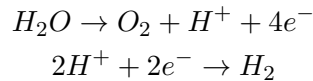
Material	Density [g/cm <sup>3</sup> ]	Tensile modulus [GPa]	Tensile strength [MPa]	Specific modulus [GPa cm <sup>3</sup> /g]	Specific strength [MPa cm <sup>3</sup> /g]
Carbon Steel S275JR	7.8	200	560	26	72
Aluminium 7075	2.8	72	540	26	192
Titanium Ti-6Al-4V	4.5	109	998	24	223
UD CFRP high strength	1.6	130	2000	81	1250
UD CFRP int. modulus	1.6	170	2400	106	1500

FIGURE 1.1: Comparison of traditional materials to CFRP (4)

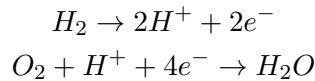
## 1.2 Fuel cell electric vehicles

This thesis is developed with the transport application of fuel cell electric vehicles in mind. The basic working principle and the place of the hydrogen storage within the system are explained below. This subsection is a more technical version of (5).

First of all, hydrogen has to be produced. The most important example of such a process is the electrolysis of water, a redox-reaction. It's important to note that this reaction needs an external energy source: electricity, preferably coming from a carbon-free source



Subsequently, the chemical energy stored in the hydrogen tank is transmitted into electricity by means of another redox-reaction, also involving oxygen coming from the air. From thermodynamics, one knows that this reaction serves as an energy supply, generating electricity



This electrical energy can then be used directly to drive an electrical motor or to charge a battery (lighter than a conventional one, (1)) that acts as an intermediate accumulator. The use of this battery allows to deal with power demand peaks and enables regenerative braking. The different flows of energy are in Fig. 1.2.

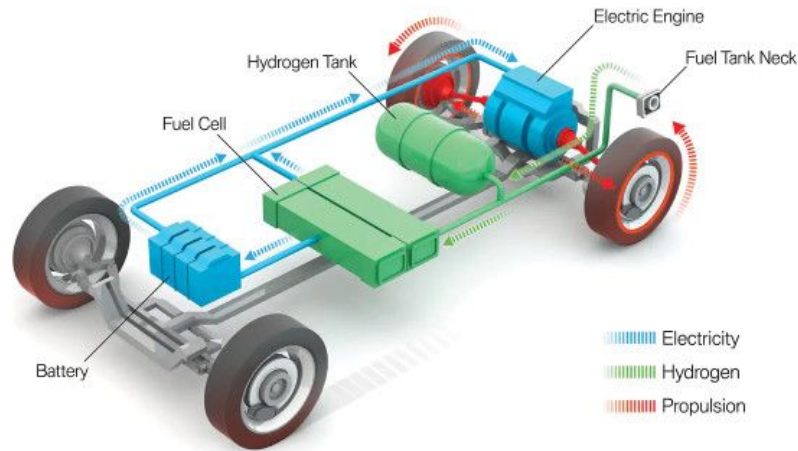


FIGURE 1.2: Different energy flows in a fuel cell electric vehicle (5)

Its main benefits are: larger range than electric vehicles, decoupled energy storage and conversion, the hydrogen tank can be refilled within minutes.

On the other hand, the efficiency of the system is inherently lower than those of electric vehicles driven by batteries because of the extra reactions to store and unleash energy to/from the hydrogen (6).

## 1.3 Composite pressure vessels

### 1.3.1 Morphology

The case-study consists of a high-pressure vessel used in fuel-cell electric vehicles to store hydrogen. Several other technologies (e.g. cryogenic liquid, foam absorption and chemical compounding) have been investigated, but high-pressure storage of hydrogen seems to be the most practical solution (8). An ISO-norm has categorised different solutions for high pressure vessels; the current envisioned solution falls under type-IV. It consists of three basic elements (see Fig. 1.3 and 1.4):

- A high-density polymer liner, which has two functions. It gives a surface to start wrapping the composite tows around, and it serves as a physical boundary to isolate the hydrogen and prevent chemical degradation.

- The composite tows, which ensure structural integrity. The wrapping consists of two modes. A first mode consists of tows that are wrapped around at an angle close to  $90^\circ$  to the cylinder axis ( $90^\circ$  would disallow the winding). These tows are called the hoop layer and support the cylindrical part of the vessel. The other mode consists of tows wrapped around the cylinder following a geodesic path. The angles that determine the path are chosen so that the nominal working condition is longitudinal tension.
- Metal inserts are placed at the ends to connect the vessel to its environment, the boss pieces.

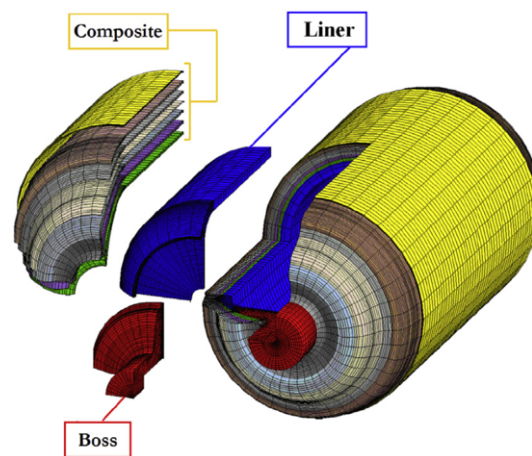


FIGURE 1.3: Full vessel morphology (7)

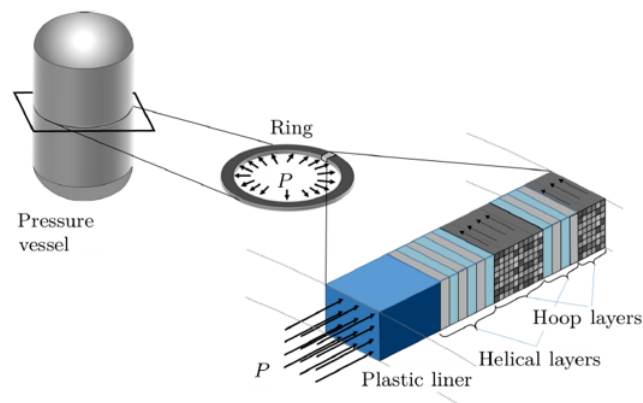


FIGURE 1.4: A more detailed view of the CPV's cylindrical part (10)

### 1.3.2 Production

This thesis is about filament wound composite pressure vessels. The filament wound production process is a technique used to produce axisymmetric components, such as a vessel. Hereunder, this production process will be briefly clarified. This subsection is a summary of (11).

The process is initiated by drawing fibers rovings from fiber creels, upon which the fibers were stored. Next, they are gathered into a band and pass a liquid resin tank containing the polymer and other chemical ingredients to acquire the suited composition in a successful way. The now resin-impregnated fibers goes to a wiping device that makes sure there is no excess of resin material. An example are two rollers whose mutual distance is controlled together with the applied tension, so that the thickness of the material that passes between the rollers can be forced. After being impregnated and wiped, the fibers are collected into a filament by the carriage. This device positions the filaments onto the rotating mandrel by making adequate movements forward and backward. The movement of the carriage determines which type of layer is being applied. After several layers are placed upon the mandrel to achieve the desired thickness and configuration, a curing process takes place. The manufacturing system can be seen in Fig. 1.6.

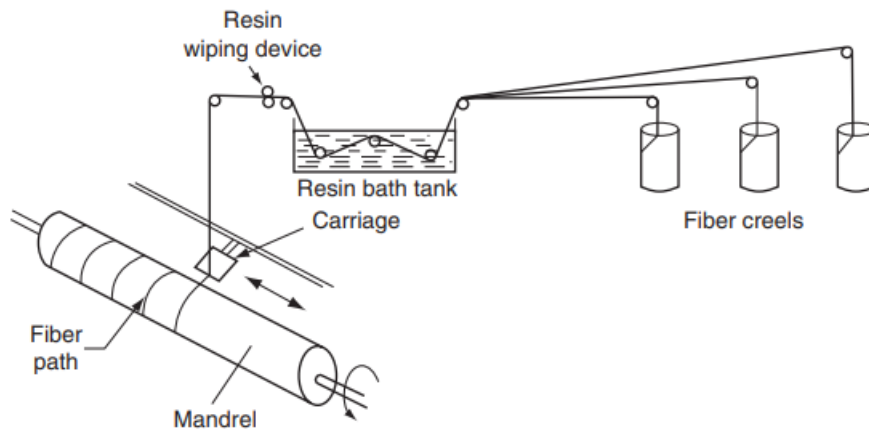


FIGURE 1.5: Different parts of the filament wound production process (12)

## 1.4 Ring test: assessing failure

The vessels are designed so that failure occurs in the hoop layer around the cylindrical part: the composite layers at the domes are thicker due to the geodesic wrapping paths. This is done because of safety issues (13). Indeed, as can be seen in Fig. 1.6, cylindrical part burst is the safest failure mode. In these circumstances, the domes are ejected inwards and not to the environment where accidents can occur.



FIGURE 1.6: Vessels burst mode: dome burst (a) and cylindrical part burst (b) (13)

Researchers have tried to make use of this fact to reduce the complexity of modelling the mechanical behaviour of the CPV (9). More concrete, they proposed to use a ring test. In this set-up a ring-like piece of the CPV is isolated and subjected to a mechanical load. The fluid pressure is approximately reproduced by an axial force applied to the ring through a radial transmission mechanism. Using this approach, the amount of testing material is greatly reduced. However, it's important to note that the ring test results can not be directly applied to model the CPV-behaviour because the axial boundary conditions are different and the geodesic wrapping influences the stress distribution at the non-cylindrical part.

The so-called ring test makes use of a the following, concrete set-up. The load source is a metallic vertical column that moves downwards. This pushes metallic segments outwards radially. Therefore, a pressure is applied to a polytetrafluorethylene (PTFE) ring. Around this PTFE ring, the CFRP specimen is placed. Consequently, the whole system is placed upon a bottom plate, which serves as a mechanical isolator towards the environment. The inherent disadvantage of the set-up is that when the segments are pushed radially, gaps initiate between the different segments. Logically, there is no longer a uniform pressure distribution; instead there is a local stress variation around these gaps that causes a bending moment. This variation can be minimized by making use of a lot of segments and the choice of the PTFE-ring. Indeed: PTFE or teflon, well-known for it's use in kitchen apparatus, shows very low friction in combination with a broad range of materials (14).



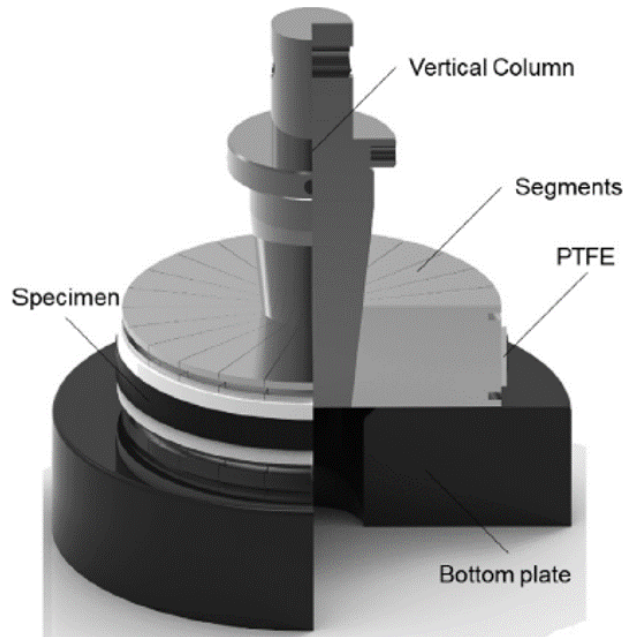


FIGURE 1.7: Set-up of the ring test (15)

Besides determining the burst pressure of the ring specimen, it is also interesting to see which failure mode occurs in the material. The load situation, but also the characteristics of the polymer and the fibre are important to assess the failure mode. To numerically determine failure occurrence, failure indices are employed.

A popular example is that of Hashin, which defines four failure modes: tensile fibre, compression fibre, tensile matrix and compression matrix. The failure mode that is expected to occur in the CPV is tensile fibre failure.

Hashin assumes a plane stress state, neglecting the stress normal to the laminate surfaces. This is certainly appropriate in the case of a CPV, since the radial stresses in a hydraulic cylinder can generally be ignored. Indeed, let's consider a thin-walled isotropic cylinder with a radius of 10 cm and a thickness of 1 cm. If the applied pressure is 35 MPa, then the radial stress ranges from -35 MPa at the inside to 0 MPa at the outside. The axial and tangential stress can be considered constant and equal to 175 MPa and 350 MPa, respectively.

Now that this assumption has been verified, the existence of a failure mode can be judged with the following Hashin-expressions (failure  $i$  is met when  $F_i = 1$ , cited from (16)):

$$\textit{”fibre tension } (\sigma_{11} > 0): F_1 = \left(\frac{\sigma_{11}}{X^T}\right)^2 + \left(\frac{\tau_{12}}{S^L}\right)^2$$

$$\textit{fibre compression } (\sigma_{11} < 0): F_2 = \left(\frac{\sigma_{11}}{X^C}\right)^2$$

$$\textit{matrix tension } (\sigma_{22} > 0): F_3 = \left(\frac{\sigma_{22}}{Y^T}\right)^2 + \left(\frac{\tau_{12}}{S^L}\right)^2$$

$$\textit{matrix compression } (\sigma_{22} < 0): F_4 = \left(\frac{\sigma_{22}}{2S^T}\right)^2 + \left(\frac{\tau_{12}}{S^L}\right)^2 + \left[\left(\frac{Y^C}{2S^T}\right)^2 - 1\right]\left(\frac{\sigma_{22}}{Y^C}\right)$$

where superscript  $t/T$  and  $c/C$  denote tension and compression;  $X$ ,  $Y$ ,  $S^L$  and  $S^T$  represent the longitudinal, transverse, longitudinal shear and transverse shear strength; the directions 11, 22 and 12 stand for on-axis longitudinal, transverse and in-plane shear stress components.”

It’s clear that several design variables and other givens (friction, width of the ring, ...) might affect the failure occurrence in the ring test. Their influence and interactions should be understood, both phenomenological and numerical. It’s also important to get an idea of which lay-ups might be expected when designing an optimal structure. Therefore different analytical and numerical techniques will be employed.

## 1.5 Conclusions

At the end of section one, it is possible to formulate the challenge this thesis is trying to tackle. Indeed, for the design of CPV’s nowadays a safety factor of 2.25 is used (2). This limits the potential weight-reduction that is realised using the composite material. A possible solution are enhanced virtual models that take into account the different design variables and other givens, based on a limited testing campaign. In this thesis, such a roadmap will be developed for a specific case-study of a high-pressure vessel used in fuel-cell electric vehicles to store hydrogen. The roadmap will base itself on the idea of a ring test and (FE-)modelling to assure a lower, but still reliable safety factor. Summarized, this introduction induces the following challenges:

- Build a nominal FE-model for the ring test that includes: realistic load condition, appropriate material behaviour, burst pressure prediction in line with test results.
- Explain the influence of the different design variables and other givens, both phenomenological and numerical.



## Chapter 2

# Nominal modelling

In this section, different models will be developed to get a reliable view of the so-called nominal situation: a ring test with an ideal, perfectly manufactured specimen. A first model is analytical; it is based on classical laminate theory. A second model consist of a FE-configuration for an elastic laminate with a hydraulic pressure. A third model gives a more realistic view: a FE-cofiguration for the actual ring test. It contains contact mechanics and an elasto-plastic model for the PTFE. This means many non-linearities are present, so a convergence analysis has been documented. The results for each model are interpreted and a comparison between the models is made.

### 2.1 Nominal situation

A clear description of the system under scope is necessary. The physical dimensions can be found on the front view depicted in Fig. 2.1. On top of that it is necessary to know that a system with 48 segments is investigated, each representing a piece of 7.5 degrees in the tangential direction. The vertical size of the column doesn't need to be known, since it is just taken to be long enough to apply the load. At first instance, results will be interpreted for a test pressure of 350 bar. The materials used for the various parts in the model and their engineering constants are summarized in Table 2.1.

Part	Material	$E_{11}[GPa]$	$E_{22}[GPa]$	$\nu_{12}$
Specimen	60% T700	250	25	0.25
	40% epoxy	3		0.375
Plastic liner	PTFE	0.4		0.46
Segment	steel	200		0.3
Column	steel	200		0.3

TABLE 2.1: Materials used in the model with their engineering constants (20)

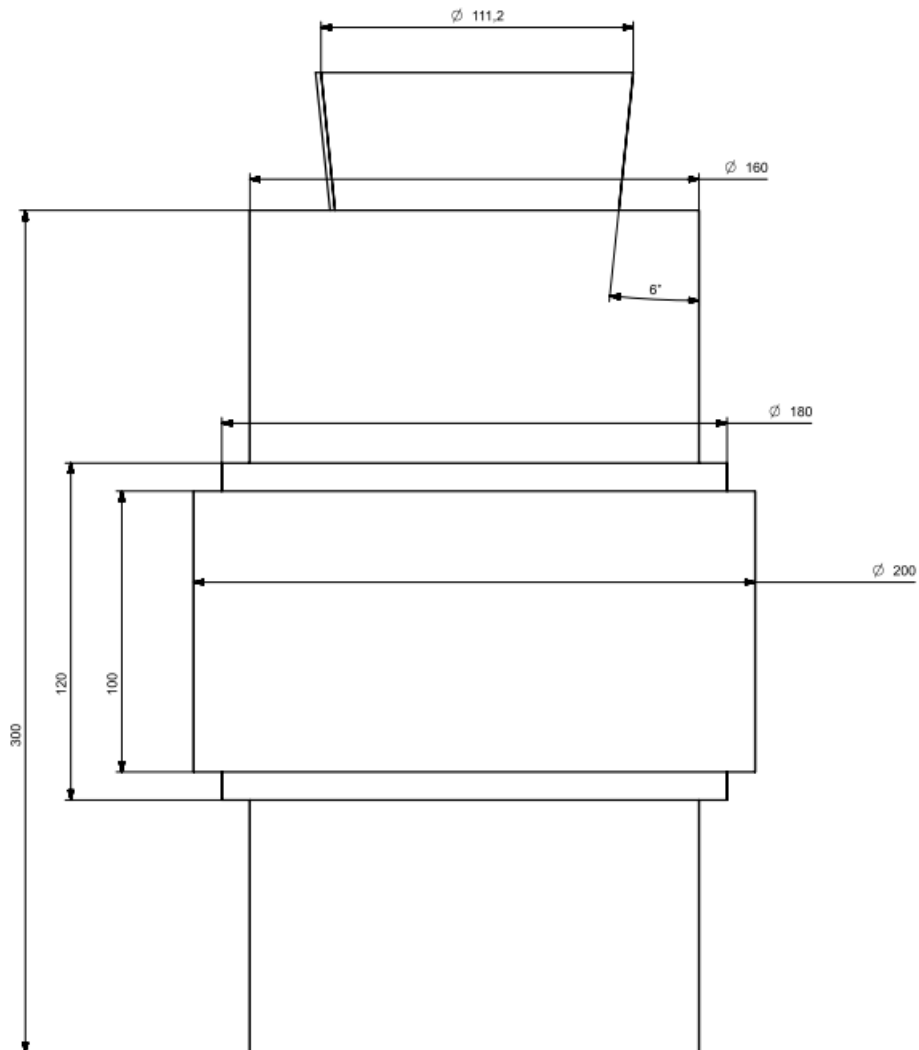


FIGURE 2.1: Technical drawing of the front view, showing the main dimensions of the ring test

The precise lay-up of the investigated specimen can be found in Fig. 2.2. Note that layer three and eight are hoop layers, so these are of particular importance. The analysis will focus on these two layers because failure is expected there.











ID		Material	Thickness	Primary Angle
10		T700/epoxy	1.000	0.0
9		T700/epoxy	1.000	45.0
8		T700/epoxy	1.000	90.0
7		T700/epoxy	1.000	45.0
6		T700/epoxy	1.000	0.0
5		T700/epoxy	1.000	0.0
4		T700/epoxy	1.000	45.0
3		T700/epoxy	1.000	90.0
2		T700/epoxy	1.000	45.0
1		T700/epoxy	1.000	0.0

FIGURE 2.2: Lay-up of the investigated specimen

## 2.2 Classical laminate theory

*This section has been composed starting from the theoretical foundation laid in (17) and a piece of code written by PhD candidate ir. Ben Van Bavel (see Appendix 5.1).*

The first, analytical model is based on classical laminate theory. This theory is based on the Kirckhoff-Love plate theory, which is based on three important assumptions:

- The different plies are perfectly bonded to each other.
- Kirckhoff hypothesis: a cross section that is initially straight and perpendicular to the neutral line, will remain so when the laminate deforms.
- The thickness of the ply remains unchanged.

The second assumption can be mathematically translated as  $\epsilon_{13} = \epsilon_{23} = 0$ . Analogous, the third assumption means that  $\epsilon_{33} = 0$ . Next, the displacements in the plane of the plate ( $xy$ ) for an arbitrary point can be calculated as:

$$\begin{aligned} u_x &= u_x^0 - z\beta_x = u_x^0 - z \frac{\partial u_z^0}{\partial x} \\ u_y &= u_y^0 - z\beta_y = u_y^0 - z \frac{\partial u_z^0}{\partial y} \end{aligned}$$

with  $\beta_i$  the angle of rotation of the normal to the neutral line; the subscript  $^0$  refers to the neutral line. An important consequence is that the displacements are only a function of one variable ( $u_z$ ). Next, strains and stresses can be calculated using these textbook relations:

$$\begin{aligned} \epsilon_{ij} &= \frac{1}{2} \left( \frac{\partial u_i}{\partial x_j} + \frac{\partial u_j}{\partial x_i} \right) \\ \sigma_{ij} &= Q_{ijkl} \epsilon_{kl} \end{aligned}$$

It is relatively easy to show that these equations can be combined to the so-called ABD-formulation, relating to the extensional stiffness (A), bending-extension coupling stiffness (B) and bending stiffness (D). Here, laminate forces and moments are given with respect to strains and curvatures, by integrating the stresses in each layer through the thickness and filling in the previous expressions for the strains:

$$\begin{aligned} \begin{bmatrix} N_x \\ N_y \\ N_{xy} \end{bmatrix} &= \begin{bmatrix} A_{11} & A_{12} & A_{13} \\ A_{12} & A_{22} & A_{23} \\ A_{13} & A_{23} & A_{33} \end{bmatrix} \begin{bmatrix} \epsilon_{11}^0 \\ \epsilon_{22}^0 \\ \epsilon_{33}^0 \end{bmatrix} + \begin{bmatrix} B_{11} & B_{12} & B_{13} \\ B_{12} & B_{22} & B_{23} \\ B_{13} & B_{23} & B_{33} \end{bmatrix} \begin{bmatrix} \chi_{11}^0 \\ \chi_{22}^0 \\ \chi_{12}^0 \end{bmatrix} \\ \begin{bmatrix} M_x \\ M_y \\ M_{xy} \end{bmatrix} &= \begin{bmatrix} B_{11} & B_{12} & B_{13} \\ B_{12} & B_{22} & B_{23} \\ B_{13} & B_{23} & B_{33} \end{bmatrix} \begin{bmatrix} \epsilon_{11}^0 \\ \epsilon_{22}^0 \\ \epsilon_{33}^0 \end{bmatrix} + \begin{bmatrix} D_{11} & D_{12} & D_{13} \\ D_{12} & D_{22} & D_{23} \\ D_{13} & D_{23} & D_{33} \end{bmatrix} \begin{bmatrix} \chi_{11}^0 \\ \chi_{22}^0 \\ \chi_{12}^0 \end{bmatrix} \end{aligned}$$

with:  $A_{ij} = \sum Q_{ij}^k (z_k - z_{k-1})$ ;  $B_{ij} = \frac{1}{2} \sum Q_{ij}^k (z_k^2 - z_{k-1}^2)$ ;  $D_{ij} = \frac{1}{3} \sum Q_{ij}^k (z_k^3 - z_{k-1}^3)$

For a composite pressure vessel, the highest stresses will occur in the cylindrical region. This can be understood by the fact that, for an isotropic vessel, stresses in the spherical domes are twice as low.

An infinitesimal part of the cylinder can be seen as a flat plate with loads  $N_{ij}$  and  $M_{ij}$  per unit length. For a thin-walled cylindrical vessel, it is well known that  $N_x = \frac{Pr}{2t}$  and  $N_y = \frac{Pr}{t}$ , while there is no shear loading. From axial symmetry, it follows that  $\chi_{ij}^k = 0$ . One can conclude that the internal bending loads  $M_{ij}$  will not influence the strains. Thus, a simplified version for this case is given by:

$$\begin{bmatrix} N_x \\ N_y \\ 0 \end{bmatrix} = \begin{bmatrix} A_{11} & A_{12} & A_{13} \\ A_{12} & A_{22} & A_{23} \\ A_{13} & A_{23} & A_{33} \end{bmatrix} \begin{bmatrix} \epsilon_{11}^0 \\ \epsilon_{22}^0 \\ \epsilon_{33}^0 \end{bmatrix}$$

After calculating these strains, the stresses in each ply can be calculated. This method had already been coded by the department (ir. Ben Van Bavel), so the code could just be used and results will be presented. A shortened version of the code can be found in Appendix 5.1.

In the interpretation of the results, the vast majority of attention will go to the tangential stresses, because these determine failure. This can be understood by referring to the isotropic case. It is well known that the radial stresses change from  $-p$  at the inner surface to 0 at the outer surface, which means they can be neglected. On top of that, it was already mentioned that the tangential stresses are twice as high as the axial stresses in the isotropic case. However, this situation is more pronounced in the case of hoop layers in a laminate wounded pressure vessel (where failure occurs). Here, the main stresses (tangential) will be the highest due to the parallel orientation of the fibers to the load. In these same layers, the orientation of the fibers is perpendicular to the axial load. Since the fibers are an order of magnitude less stiff in this direction, only a small amount of the axial load will be beared by the hoop layers.

The results of the model are shown in Table 3.1. For the sake of completeness, both tangential, axial and shear stresses are given. As predicted, the tangential stresses are dominant and attain a maximum in the hoop layers of 875 MPa.

Ply ID [degrees]	1	2	3	4	5	6	7	8	9	10
Tangential	94	287	875	287	94	94	287	875	287	94
Axial	303	113	50	113	303	303	113	303	113	303
Shear	-91	116	91	116	-91	-9	116	91	116	-91

TABLE 2.2: Results of the analytical model per layer, all stresses are in MPa



## 2.3 Elastic composite, subjected to hydraulic pressure (FE)

The next model will be the first finite element model of this thesis. It has been made with software from Siemens: Simcenter 3D as pre- and post-processor, Nastran NX as processor. The situation that will be modelled is that of an elastic composite, subjected to an internal hydraulic pressure of 350 bar. Dimensions and material choices are identical to those of the previous model. First the build-up of the model will be elaborated in four bullets (**Purpose, Meshing, Boundary Conditions, Load**) and subsequently the results will be discussed in a complete manner.

### 2.3.1 Development of the model

#### **Purpose**

A structural analysis is done using the solver SOL 101 Linear Statics. The goal is to make a finite element model of the analytical formulation. In this way, the differences between the analytical and numerical model can be investigated. It also serves as a stepping stone for a more complicated model of the actual ring test.

#### **Meshing**

The ring has been meshed using eight-noded hexahedral elements. This is a compromise between efficiency and accuracy: while tetrahedral elements are often too stiff, the first order hexahedral element is assumed to be good enough since the load case is simple and the meshing fine enough (18). The size of each element is 10 mm (axial) by 10 mm (tangential) by 1 mm (radial). Since only one quarter of the ring has been simulated to save computation time, a model with 3960 nodes is attained.

#### **Boundary conditions**

Axisymmetry should be included; the rigid body motions should be prohibited. Both can be implemented by means of three boundary conditions. First, the three translating degrees of freedom of all the nodes in one of the cutting planes have been coupled with their equivalent counterpart in the other cutting plane. This is equivalent to disabling movement into the symmetry plane to enforce the symmetry condition. Secondly, one single node in the cutting plane has been restricted in the axial direction. The third condition is the restriction of another node, positioned straight above the node that was mentioned earlier, but now the restriction is in the radial direction.

The completeness of these conditions can be understood in the following way. By the axial restriction, axial rigid body motion is restricted. By the radial restriction, the radial rigid body motion is restricted, but also the tangential body motion by means of the node coupling. Similarly, also the three rotational degrees of freedom for rigid body motion are prohibited using this set of boundary conditions.

### Load

The load situation is rather trivial: a hydraulic, internal pressure of 350 bar is applied to the ring.

In Fig. 2.3 one can find a graphical representation of the model presented here.

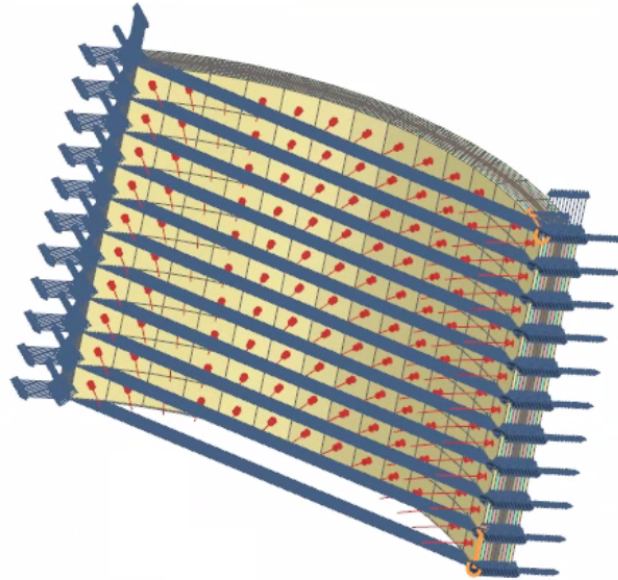


FIGURE 2.3: Figure of the finite element model. Load and boundary conditions are depicted: the load is in red, the coupling conditions in blue and the translating restrictions in orange

### 2.3.2 Solution of the model

The model has been simulated, its computation time was less than ten seconds. First, the different reaction forces and moments have to be checked: they should be negligible, otherwise the system is overconstrained. In Fig. 2.4 it is shown that the reaction forces are as expected. The reaction moments are exactly zero so they are not shown. Next, the main results are checked upon their physical validity: the stresses are investigated, with a focus on the tangential ones.

First, the radial stresses are looked upon. Based on the physical situation, one expects a quasi-homogeneous image across the ply, ranging from -350 bar at the inner side to 0 bar at the outer side. The actual image (Fig. 2.5) is in line with the expectations. However, in each layer there are different bands with a slightly different tangential stress (the inner layer is depicted in Fig. 2.5). This difference with the theoretical case of a cylindrical section can be explained due to its finite length: there is some curving at the edges. Indeed, the same effect has been noted in a finite element simulation of an isotropic ring. For the tangential stresses, different phenomena can be observed in Fig. 2.7. It is in line with expectations to see that the tangential stresses get higher when the fibers are directed more in this direction (= hoop layers). The stresses get less high outwards, which is also the case for the analytic solution of an isotropic cylindrical section with a non-neglectable thickness. On top of that, it is noted that the stress in each layer is a bit higher in the center, which can again be explained due to the curving by the finite thickness (depicted for the inner hoop layer in Fig. 2.8).

The last stresses that should be discussed are the axial stresses. This behaviour is less trivial, as can be seen in Fig. 2.10. A starting point to explain it, is that the total axial stress at each axial cutting plane sums to zero. This has been verified experimentally and is logical given the load state which does not contain an axial component. Since the layers are well-bonded, axial stresses will be distributed in such a way so that the layers displace together while maintaining a total axial stress of zero. This means that both compressive and tensile stresses are observed in the axial direction. Similar to the tangential stresses, also the axial stresses decrease outwards. Again, curving effects are encountered due to the finite length of the ring within each layer (illustrated for the inner layer in Fig. 2.11).

2.3. Elastic composite, subjected to hydraulic pressure (FE)

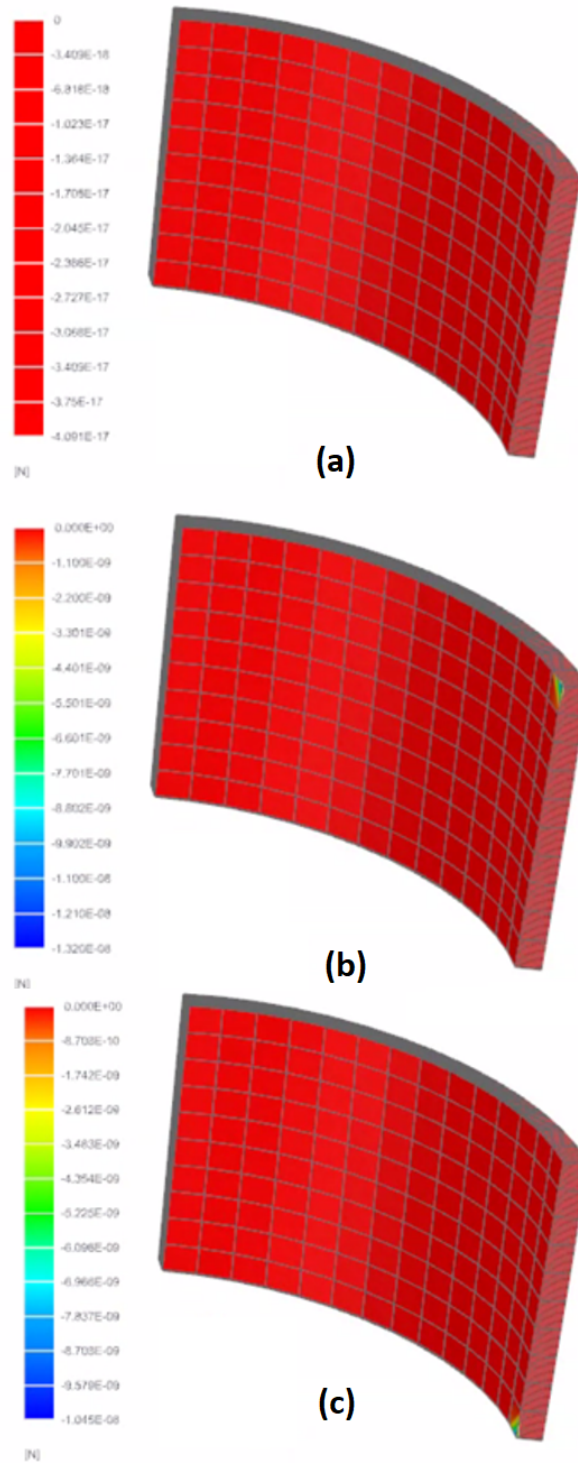


FIGURE 2.4: Reaction forces (a) radial forces (b) tangential forces (c) axial forces

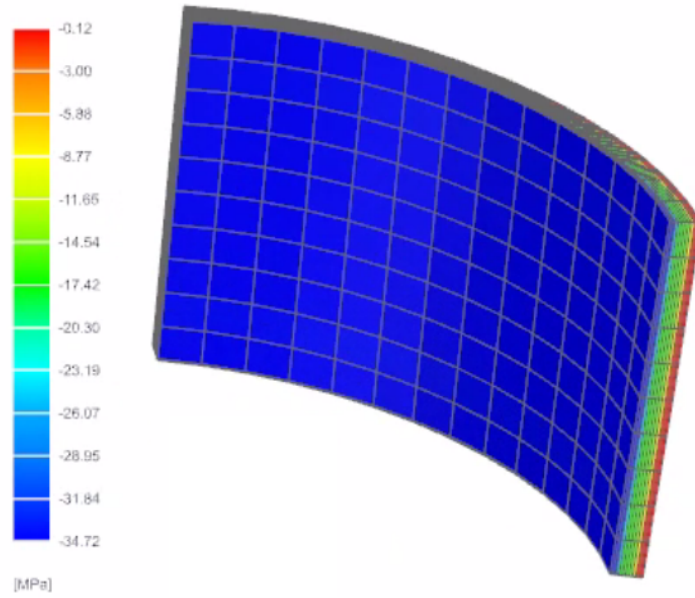


FIGURE 2.5: Radial stresses in the different plies.

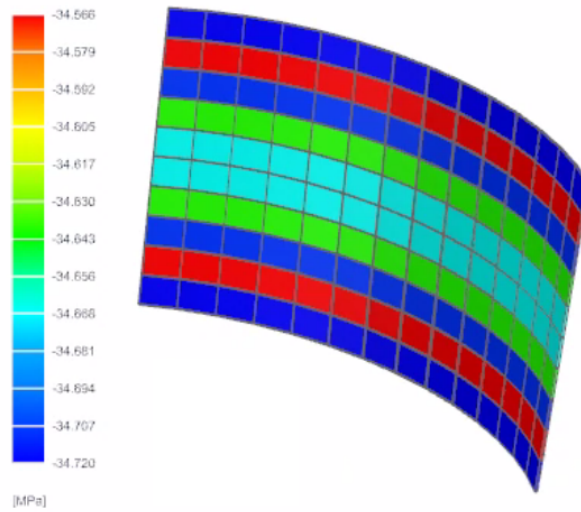


FIGURE 2.6: Radial stresses at the inner layer, bands are observed due to curving by the finite thickness

### 2.3. Elastic composite, subjected to hydraulic pressure (FE)

---

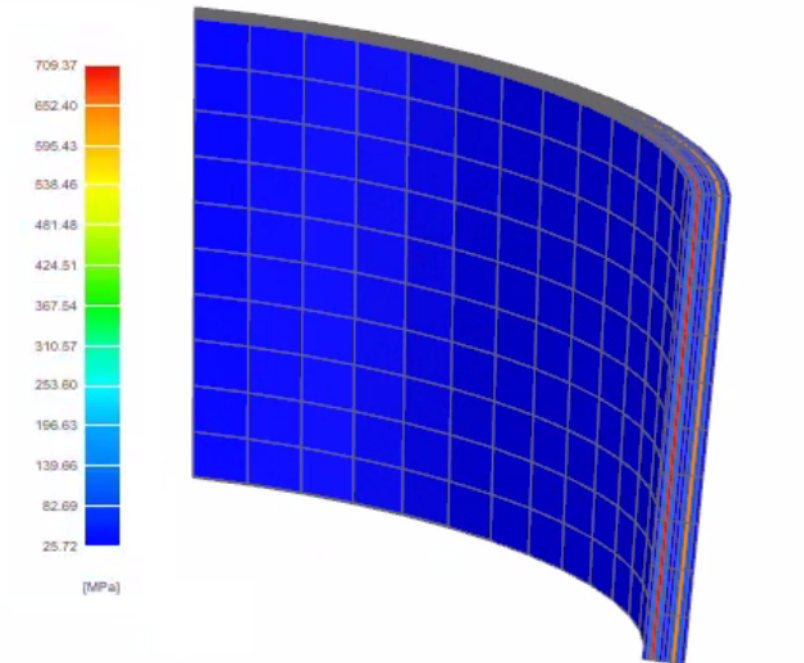


FIGURE 2.7: Tangential stresses in the different plies

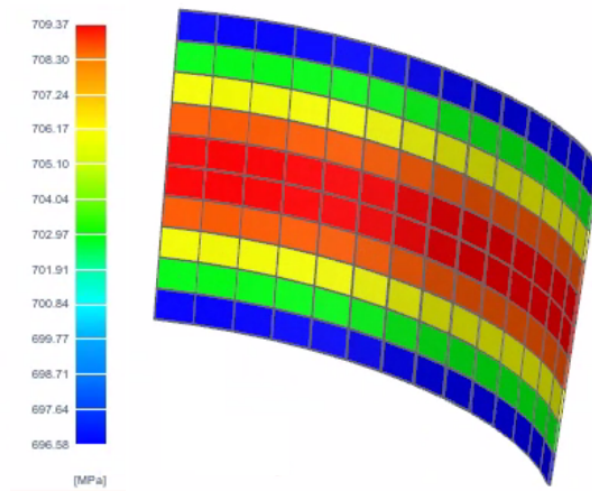


FIGURE 2.8: Tangential stresses at the inner hoop layer, stresses at the center are a bit higher

### 2.3. Elastic composite, subjected to hydraulic pressure (FE)

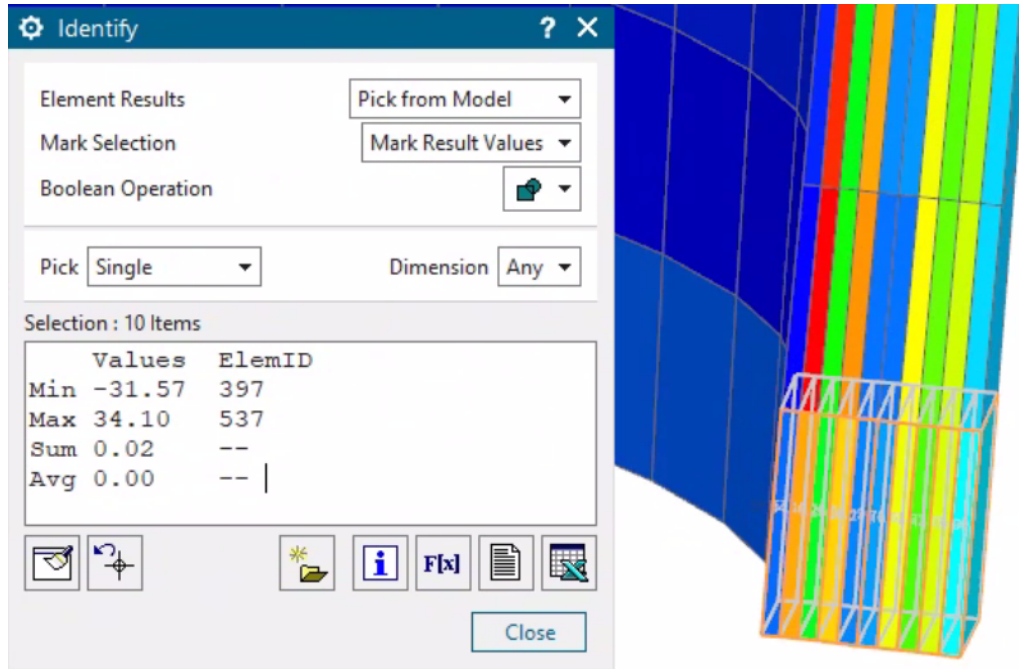


FIGURE 2.9: Part of the experimental validation of the fact that the axial stresses sum to zero at every cutting plane

To end this section, the maximal tangential stresses in each layer are summarized in Table 3.1. This information will be restated when a comparison is made between the different models.

Ply ID	1	2	3	4	5	6	7	8	9	10
[degrees]	0	45	90	45	0	0	45	90	45	0
Tangential	26	198	709	184	30	30	159	639	153	15

TABLE 2.3: Results of the first, simplified FE-model per layer. All stresses are in MPa

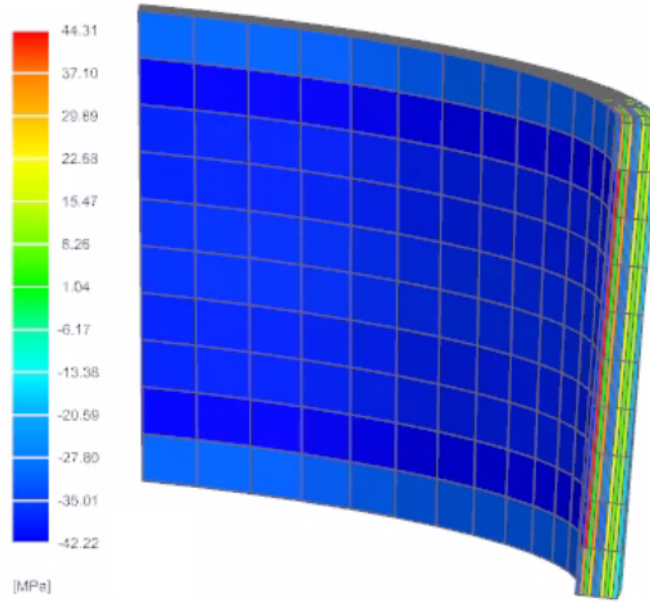


FIGURE 2.10: Axial stresses in the different plies

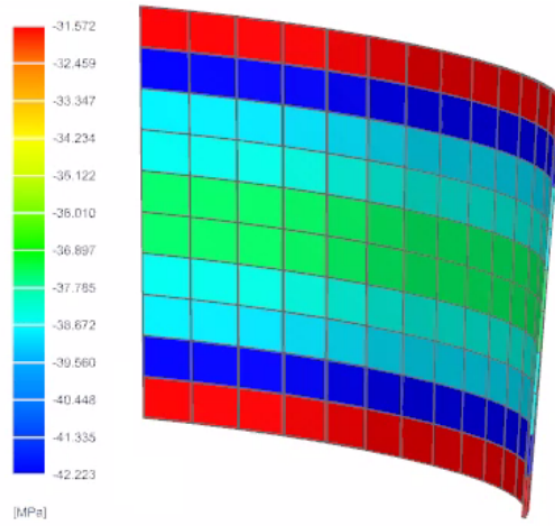


FIGURE 2.11: Axial stresses at the inner layer, bands are observed due to curving by the finite thickness



## 2.4 Imitation of the ring test mechanisms (FE)

The last step in the development of a nominal model is to include the contact mechanism to transfer the load and perform an elasto-plastic analysis on the liner material. This will be done in the third and final model of this section. Again, dimensions and material choices are reused. The build-up of the model will be explained using six bullets: **Purpose, Meshing, Boundary Conditions, Load, Contacts, Plasticity**. Subsequently, the results will be clarified and physical plausibility will be shown. Lastly, a convergence analysis will be presented to check whether the many non-linearities in the model do not cause unphysical side-effects.

### 2.4.1 Development of the model

#### **Purpose**

A structural analysis is performed using SOL 401 Multi-Step Nonlinear. The goal is to make a finite element formulation of the actual ring test set-up. In a later stage, it will be investigated which parameters are key to determine the results of the ring test with respect to an actual usage case.

#### **Meshing**

It is important to note that the modelled ring test consists of 48 segments. To save computation time only two segments have been modelled ( $15^\circ$  of the model), containing all the necessary information since the envisioned realization of the ring test is cyclic with respect to the tangential direction. For the different components, varying element sizes have been used depending on how critical the part is estimated towards the failure determination. The vertical cone and the segments are only necessary to achieve a realistic contact pressure image (by forming gaps between the different segments). As will be shown later, this could already be realised using three tangential layers (of five degrees), consisting of 20-noded hexahedral elements with dimensions of 100 mm by 100 mm. The choice for second order elements was made to allow bending of the big elements, which was considered to be more appropriate in this case than a finer first order mesh with elements that could not bend. This means that the vertical cone and segments have been modelled using only 420 nodes. Next, the plastic liner is meshed using 30 layers (half a degree each) of eight-noded hexahedral elements with dimensions of 2.5 mm by 2.5 mm. It is clear that the liner elements have been made finer in the tangential direction to model the effect of the bending moments, initiated by the forming of gaps. This makes for a total of 7596 nodes. Finally, each layer of the laminate has been drawn using eight-noded hexahedral elements of 2 mm by 2 mm, good for a total of 27540 nodes to represent the laminate.

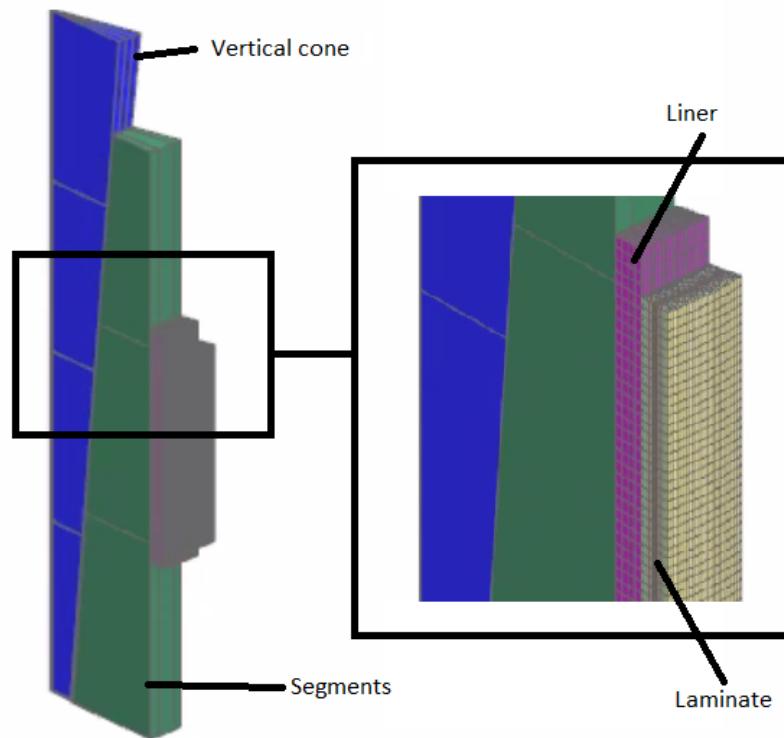


FIGURE 2.12: Figure of the FE-model of a ring test of 48 segments, different parts with appropriate mesh sizing are shown. All the necessary information is present in a slice of 15 degrees

#### **Boundary conditions (see Fig. 2.14)**

The ground has been simulated by disabling the axial movement of the nodes down below the segments. Next, the tangential movement of the nodes at the side of the model have been disabled: for the vertical cone, for the segments and for the plastic liner. The equivalent nodes for the laminate have been coupled, so as to allow for rotation of the laminate due to the loading. Lastly, the central nodes of the central segment have been restricted not to move tangentially.

This is equivalent to defining the tangential contact between the different segments, but saves quite a meaningful amount of time. Indeed, by disabling the movement of these nodes, the central segment is prohibited from moving so it will realize pushing/pulling contact with the other segments. In this way, also the cyclic and symmetric character of the solution is guaranteed. This will also be checked later on.

**Load**

The load has been defined in a way that may seem unusual at first sight: the axial movement of the nodes at the top of the vertical cone have been defined as -10 mm. This has been done because it is computationally more stable to define a movement instead of a pressure. It will be shown that the choice of -10 mm corresponds to a contact pressure of about 350 bar between the segments and the plastic liner, although this is a bit ambiguous because the pressure is no longer homogeneous. Since the definition of the load has to include the factor time, the load has been applied in 20 steps of each 0.1 second.

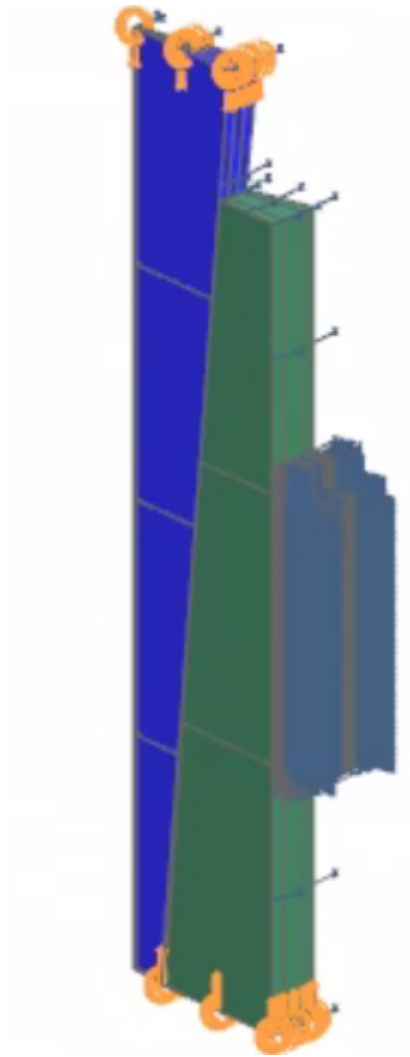


FIGURE 2.13: Indication of the boundary conditions and load: tangential constraints are in blue, axial constraints in yellow

### Contacts

There remain several contacts that have to be defined: the vertical cone pushing the segments outwards, the segments then pushing the PTFE-layer along and the liner pushing the laminate in the same direction. Each time, a source and a target region have to be chosen. It is computationally the most interesting to choose the most rigid surface as the source. This is because the source elements can penetrate the other surface, while the target elements cannot. By choosing the rigid surface as the source, the 'fictive' penetration into the most rigid surface is prohibited.

On top of that, friction coefficients have to be provided for the different contacts. For the contacts involving the liner, coefficients of 0.2 have been chosen. A sensitivity analysis will happen in a later stage, because these coefficients are not well-known. The coefficient between the steel surfaces is less important, since it is only the goal to reproduce a realistic contact pressure at the liner so the stress distributions in the steel components do not really interest us. However, it is obvious that the force transmission will be less efficient if high friction is present between the two steel surfaces. The pressure field applied to the ring will thus have the same shape, but will be at a lower level for high friction.

### Plasticity

A last addition to this model is to include the plastic behaviour of the liner. This is necessary since the PTFE material will show plastic behaviour almost immediately. For this feature, the definition starts from uni-axial tensile tests (19). The tests are performed for different strain rates, but since it takes several minutes to fill a CPV, it can be assumed that the slowest curve is the most appropriate. On top of that, a yield criterion with associated flow rule has to be selected. The standard Von Mises-criterion for ductile materials has been chosen.

### 2.4.2 Solution of the model

After implementing these features, the simulation took place. The simulation lasted over one hour. This can be explained by the size of the model (over 20000 nodes) and due to the fact that the load is applied in 20 steps, each taking around ten iterations to get the contacts to converge. This means that the matrix system has to be solved around 200 times.

The simulation time can be reduced by only taking one half of the system. However, at first instance the choice has been made to go with the full system. In this way, an extra control mechanism is included: the system should show symmetry.

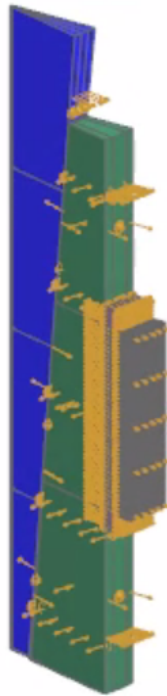


FIGURE 2.14: Indication of the contact definitions in yellow

Before actually looking at numerical results, it should be checked that the general image of the displacements are as expected. In particular, interest goes to the gap initiation between different segments. Additionally, the liner should bend around the laminate. The first effect is observed in Fig. 2.15 and in Fig. 2.16. Note that the displacements have been greatly exaggerated to make them more clear. The same goes for Fig. 2.17 and 2.18, in which the bending of the liner around the laminate can be noticed. With the help of these figures, one can also visualize the transmission mechanism, consisting of the vertical column moving downwards, pushing the segments outwards.

A first numerical result that should be checked is the contact pressure at the inside of the liner. While in the previous model a homogeneous pressure was applied, here a more complex image is attained. It can be seen in Fig. 2.19, in which both the contour plot and some local pressure profiles are shown.

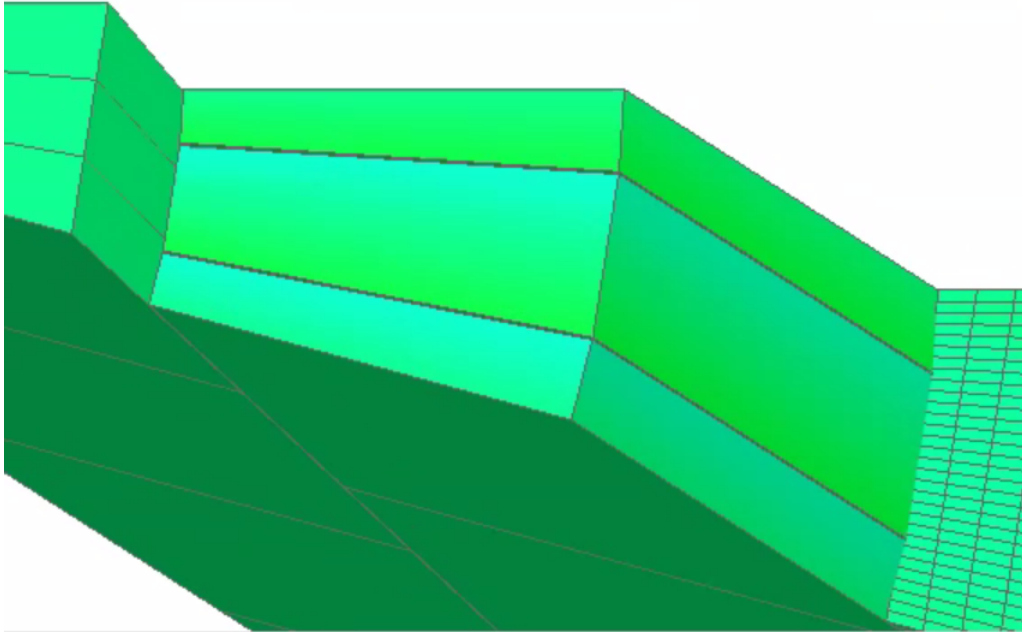


FIGURE 2.15: Initiation of the gap: at the start, colours refer to tangential movement

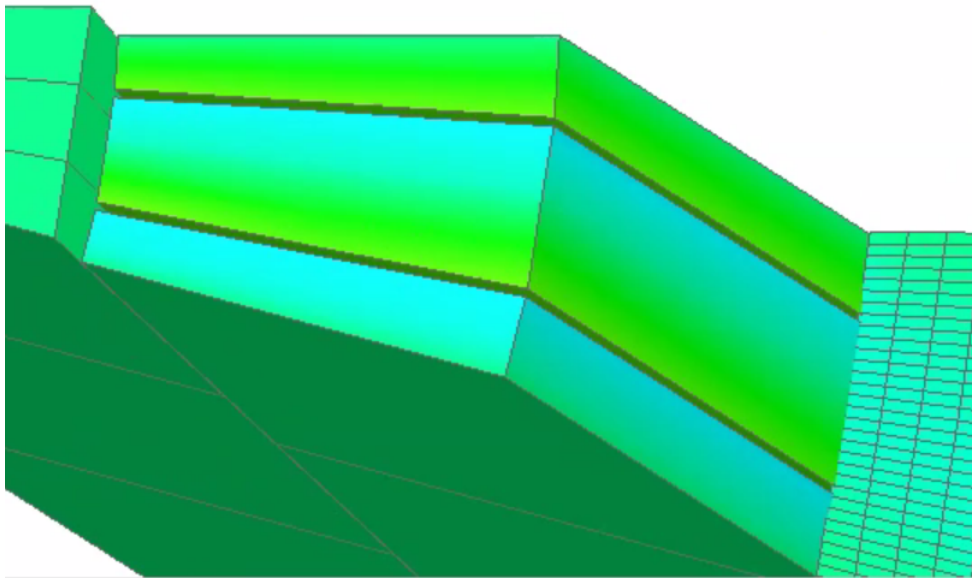


FIGURE 2.16: Initiation of the gap: at the end, colours refer to tangential movement

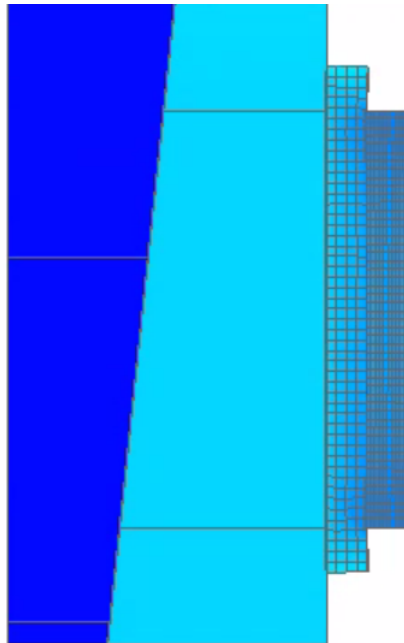


FIGURE 2.17: Bending of the liner around the laminate: at the start, colours refer to radial movement

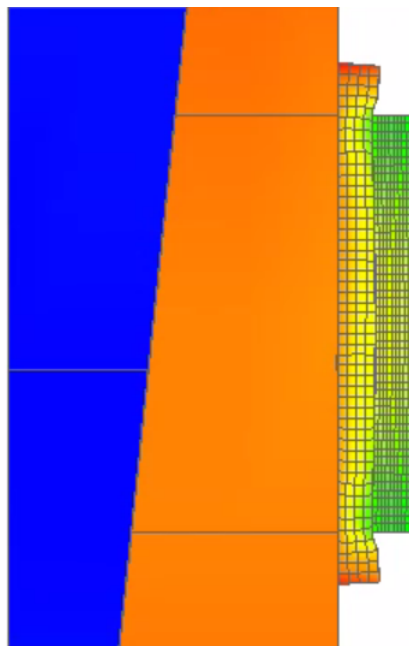


FIGURE 2.18: Bending of the liner around the laminate: at the end, colours refer to radial movement

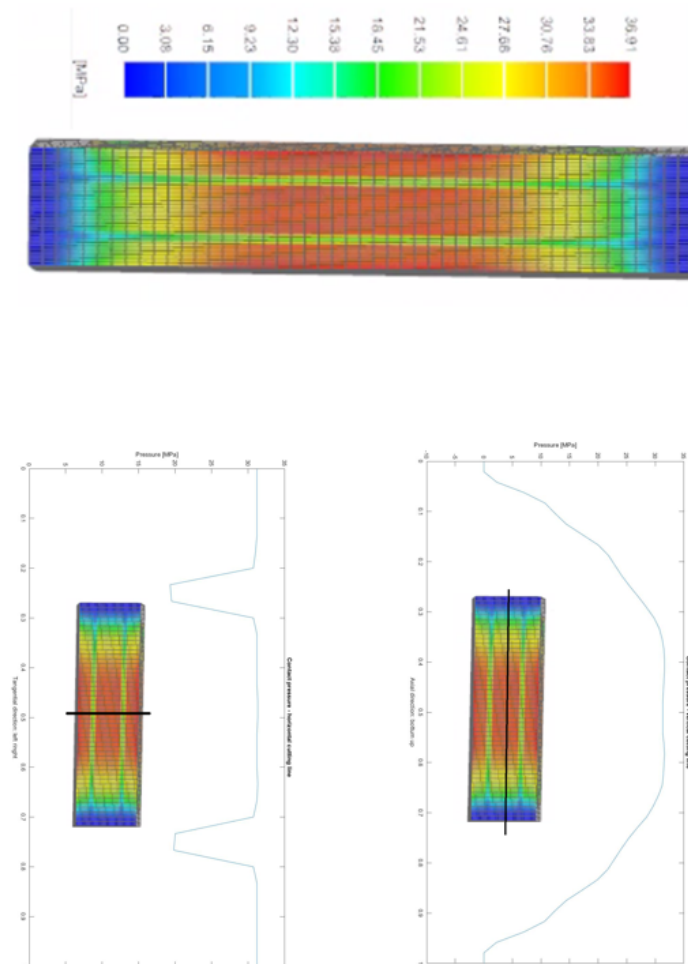


FIGURE 2.19: Analysis of the contact pressure: contour plot, horizontal profile, vertical profile

The pressure at the horizontal center line is 312 bar, with a sudden decrease at the gaps down to 195 bar. On the vertical center line, the effect of the axial width of the setup can be seen: it varies from the normal value down to zero bar at the edges, as expected. Note that the value from 312 bar is not equal to the 350 bar of the previous models, because it is not that easy to predict this pressure based on the vertical displacement of the cone. This side-note will be included when a comparison is made with the other models.



## 2.4. Imitation of the ring test mechanisms (FE)

The next step is to look at the actual stresses in the composite. Because it has been extensively shown already that attention should go to the tangential stresses in the inner hoop layer, only plots of this stress in this particular ply will be shown. However, maximum tangential stresses for all the plies will be reported briefly. Also, different stress profiles at certain cutting lines will be shown, together with the contour plot. In this way, a complete image is achieved: visual and numerical.

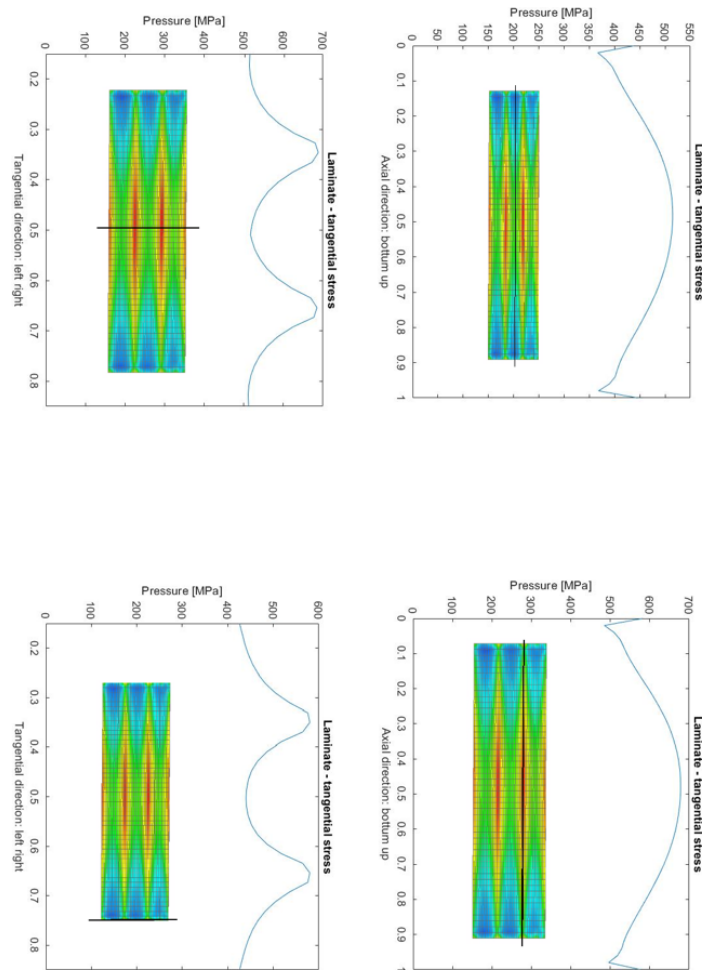


FIGURE 2.20: Different stress profiles in the inner hoop layer, together with the contour plot

Different profiles representing tangential stresses in the inner hoop layer are plotted in Fig. 2.20. Again, the effect of the rather wide ring can be seen in the axial profiles: the maximum can be found in the middle, then the stress goes down towards the sides. At the sides, an interesting side-effect occurs due to the bending of the liner around the laminate. Indeed, the decrease stops and a rather sharp increase is detected, forming a local minimum. On the tangential profiles, the main remark that should be made is that the local valley of the pressure load causes a local peak in the tangential stress. On all figures, symmetry is present.

Hereunder the maximum tangential stresses in the different plies are stated, this will serve for a comparison between the different models later on:

Ply ID	1	2	3	4	5	6	7	8	9	10
[degrees]	0	45	90	45	0	0	45	90	45	0
Tangential	53	174	688	187	45	47	131	638	156	50

TABLE 2.4: Results of the second, more complex FE-model per layer. All stresses are in MPa.

### 2.4.3 Failure determination

The next phenomenon about which interesting statements can be made is the occurrence of failure. In the context of this thesis, only first element failure will be evaluated using the failure indices of Hashin that were introduced in subsection 1.4. This means that no progressive damage law is implemented. Physically, this comes down to the assumption that structural failure occurs immediately after first ply failure. This assumption can be motivated by the fact that the composite is a very brittle material. Additionally, multiple authors have concluded that the initial damage does cause the final failure (21) (22).

These are the relevant properties to calculate the Hashin indices for the case of a T700/epoxy-composite:

$X^T$	$X^C$	$Y^T$	$Y^C$	$S^L$	$S^T$	$Y^N$	$Y^S$
2500	1250	60	186	85	85	60	85

TABLE 2.5: Strength parameters for T700/epoxy composites, values in MPa (23)

Based on these values and the local stresses, the indices can be calculated. Normally, this can be automated using the software. However, Solver 401 does not allow to use the elements that enable this (PCOMPS). This means the calculations had to be done by the author himself. Herefore, the stresses had to be converted from a local cylindrical coordinate system into a coordinate system that is aligned with the fibre. This can be easily done by means of a rotation around the radial axis over an angle of 90 degrees minus the orientation of the ply.

In this way, the first node that would fail (= failure index equal to one) could be identified by augmenting the load until a node appeared at which the failure criterion was met. The node where this first happened was the one with node ID equal to 195726. The next step was to determine the failure mode, the burst pressure and the location of this node.

The location of the node is in the inner hoop layer, at the middle of one of the gaps. Its precise location is depicted in Fig. 2.21.

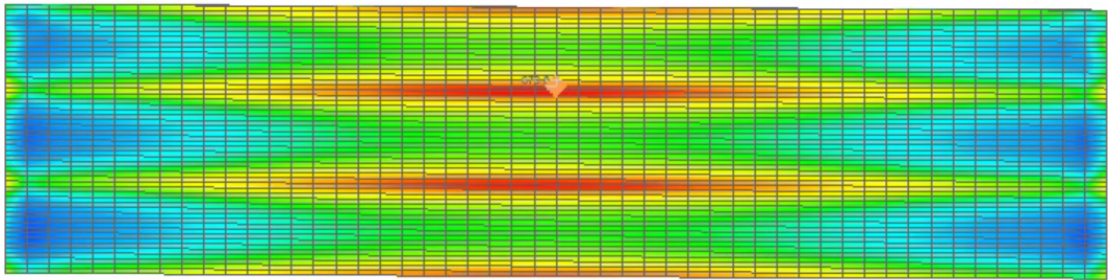


FIGURE 2.21: Location of node 195726, where failure initially occurs

The value of the different failure indices allow to determine the failure mode. They are listed hereunder for the particular node. As can be seen, the failure mode that will occur is matrix tension.

fibre tension	0.23
fibre compression	not applicable
matrix tension	1.00
matrix compression	not applicable

TABLE 2.6: Failure indices for node 195726, the failure criterion used is Hashin

The burst pressure at which the failure criterion is first met equals 380 bar. This is a reasonable value, taking into account that the ring is rather thin and that the lay-up has not been optimised.

#### 2.4.4 Convergence study

Because of the many non-linearities in the system, it was important to check whether the solution was numerically converging before performing further analysis.

There are different parts in the system. Firstly, there are the vertical column and the segments. Because their only goal is to imitate the contact pressure at the inner side of the liner, a very rough mesh already suffices: the stresses in these components are not of particular interest. That's why a convergence analysis is not necessary for them.

The next component is the liner. Here a convergence analysis for the tangential stresses in the inner hoop layer is relevant. Again, the suited stress profiles will be shown together with the suited contour plot. The analysis for a changing number of nodes in the liner can be found in Fig. 2.22.

The legend can be explained as follows: the simulation with  $n = 1$  has the mesh dimensions of the nominal model. A model with  $n = 1.25$  means that all the dimensions of the liner mesh have been divided by 1.25, resulting in a finer mesh. Simulations have been performed for  $n = 0.5$ ,  $n = 0.75$ ,  $n = 1$  and  $n = 1.25$ . As can be seen, convergence is achieved very fast and in a solid manner. The only noteworthy evolution are the valleys at the axial edges that become less smooth and more abrupt for finer meshes. This is logical since the real distribution is smooth, but can only be represented accurately if there are enough nodes, since the variations are quite strong and local.

In Fig. 2.23 and Fig. 2.24, the same approach was taken, but for the number of nodes of the laminate in the tangential direction. The number of nodes in the tangential direction is reported in the legend:  $n = 15$ ,  $n = 30$ ,  $n = 45$  and  $n = 60$ . Convergence is achieved much slower: the graph becomes a lot smoother for finer meshes and the peak at the gap rises a bit. The finer the mesh, the smaller the difference between consecutive meshes.

Next, the number of nodes in the laminate in the axial direction was also varied. The following simulations have been run:  $n = 15$ ,  $n = 30$  and  $n = 45$ . The results can be found in Fig. 2.25 and Fig. 2.26. Again, fast convergence is achieved. Like before, some variation on the axial edges can be observed. The finer the mesh, the more the valley displaces towards the edge; the valley also gets sharper.

After interpreting the results of the FE-model and performing the convergence analysis above, good confidence can be put in the model. However, a comparison with the previous models is still necessary to further increase trustworthiness.

## 2.4. Imitation of the ring test mechanisms (FE)

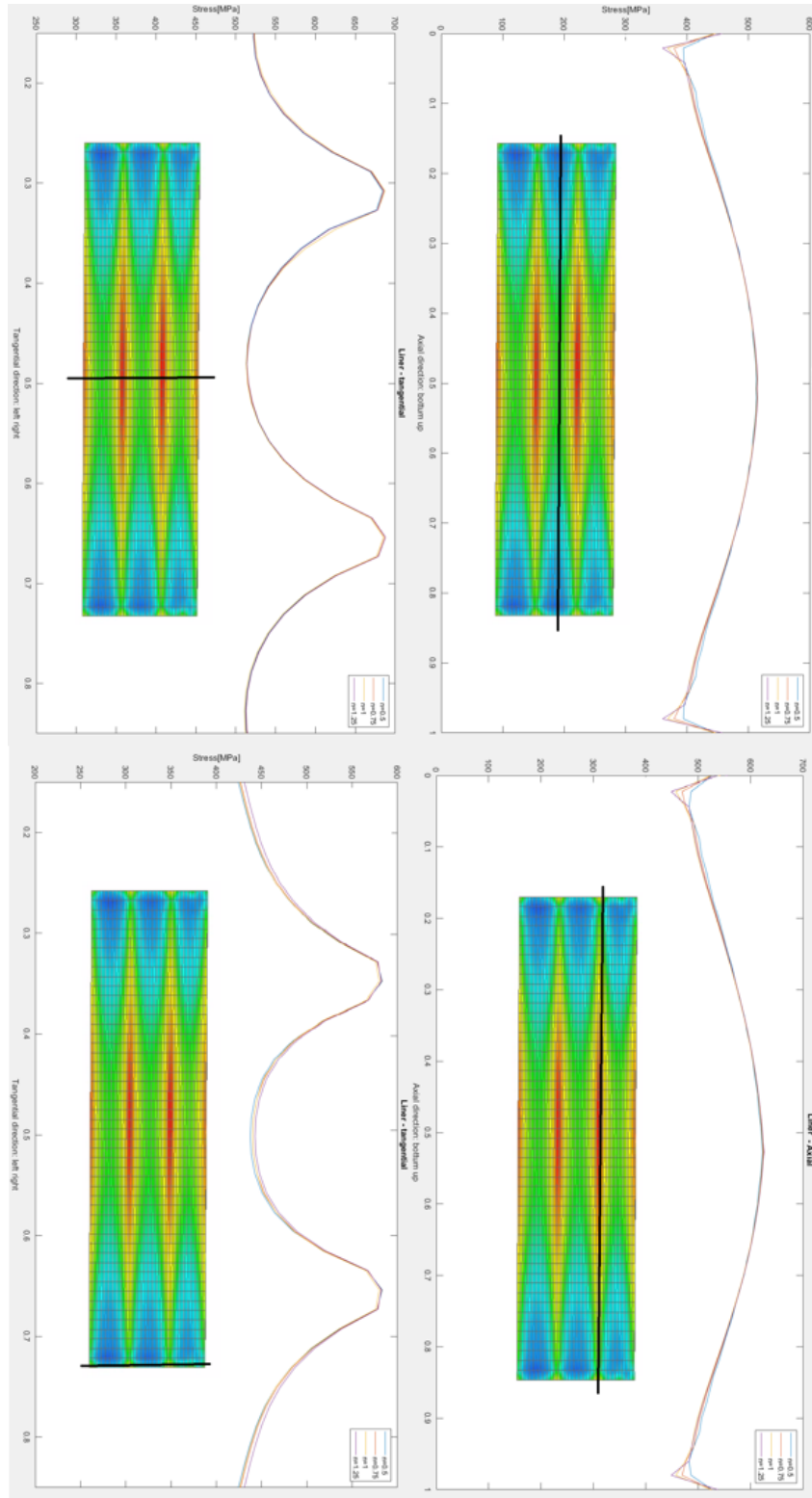


FIGURE 2.22: Convergence analysis: a varying number of nodes in the liner

## 2.4. Imitation of the ring test mechanisms (FE)

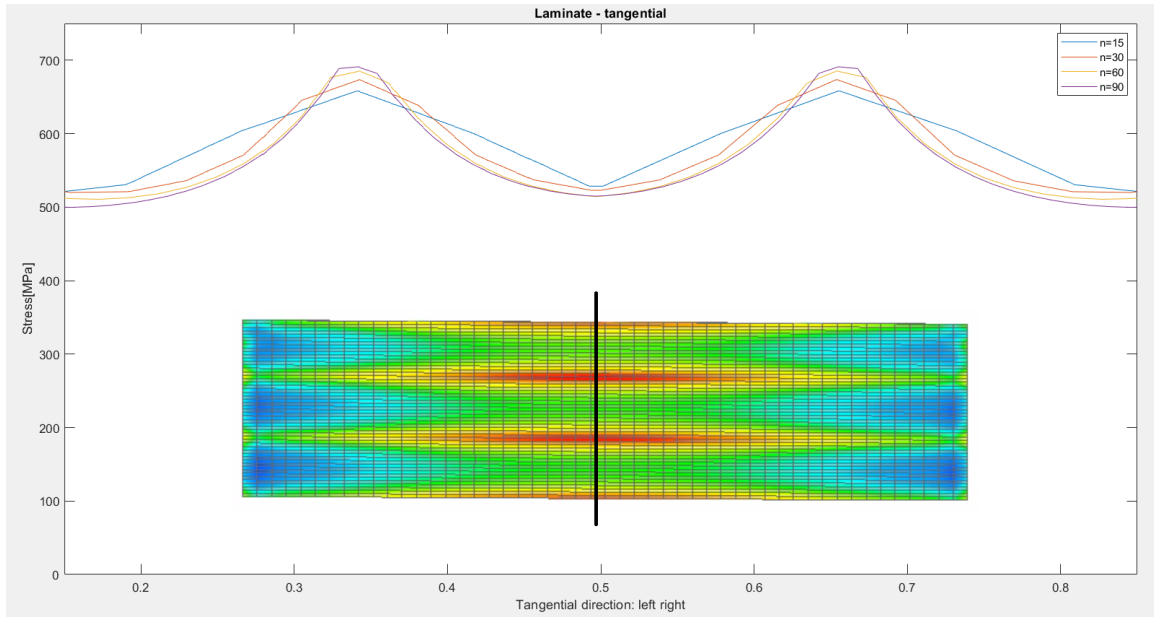


FIGURE 2.23: Convergence analysis: a varying number of nodes in the laminate, in the tangential direction

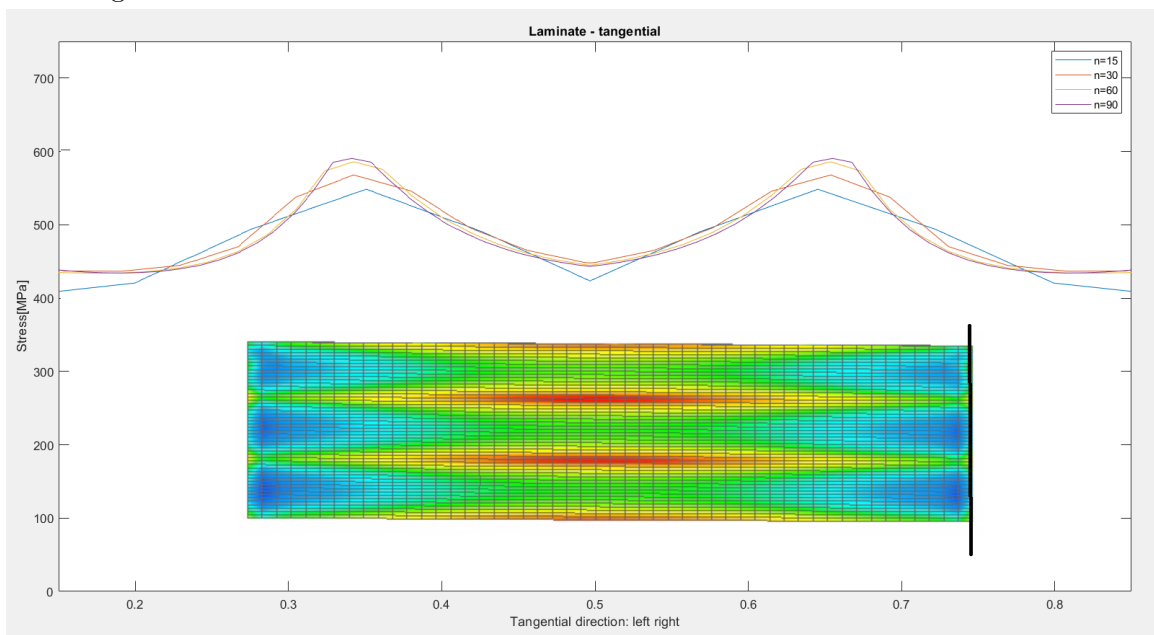


FIGURE 2.24: Convergence analysis: a varying number of nodes in the laminate, in the tangential direction

## 2.4. Imitation of the ring test mechanisms (FE)

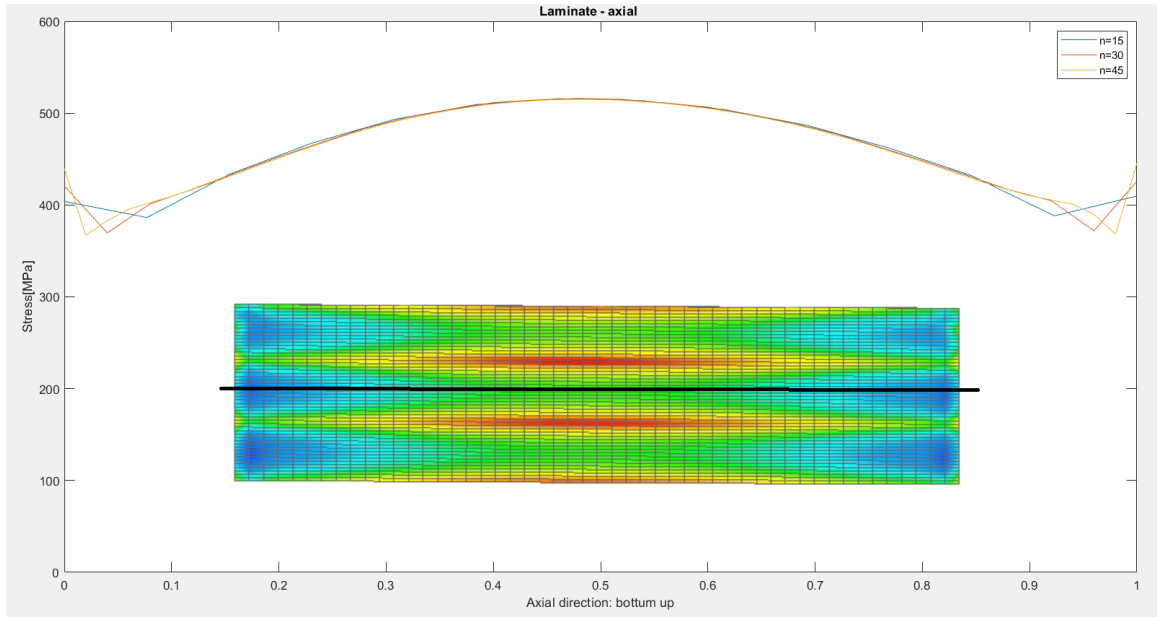


FIGURE 2.25: Convergence analysis: a varying number of nodes in the laminate, in the axial direction

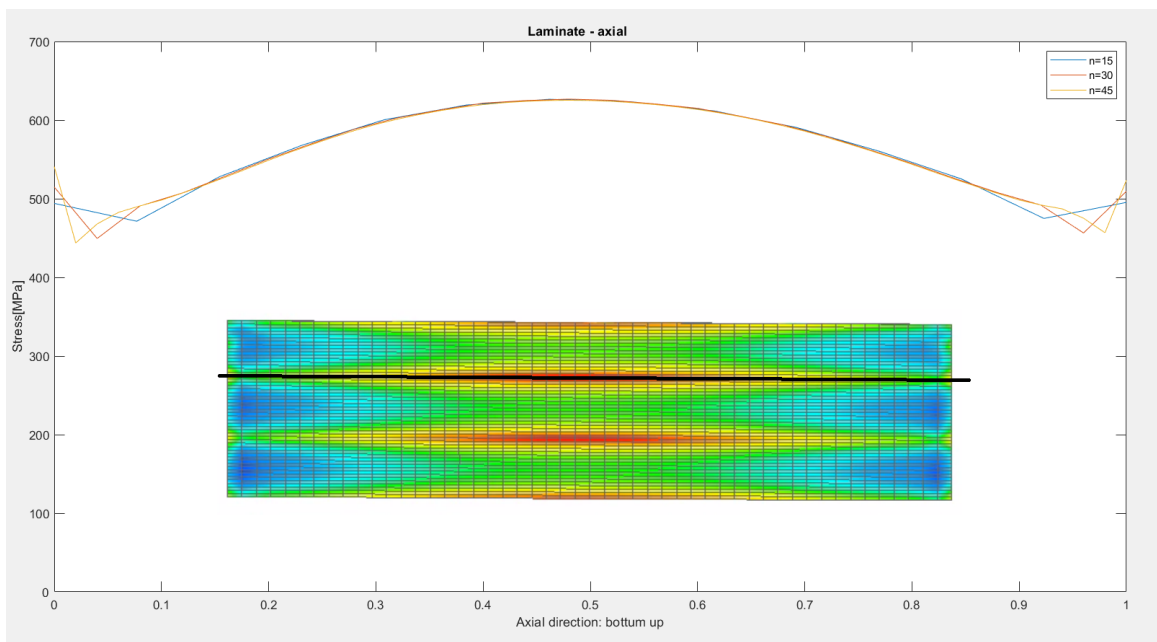


FIGURE 2.26: Convergence analysis: a varying number of nodes in the laminate, in the axial direction

## 2.5 Conclusions

In this chapter, a setup with an example ring test with accompanying lay-up has been used to illustrate the development of models to predict the mechanical response of the mechanism. First, an analytical model was developed based on classical laminate theory. Secondly, a simplified finite element model was used to see whether the results of the first model could be replicated by a numerical model. Lastly, an extensive finite element model was developed to fully demonstrate the results than can be expected in a ring test. This model contained advanced features such as plastic behaviour, contact mechanisms, failure indices, ... Besides showing the expected displacements, the model can be used to do numerical statements.

A comparison between the models can be done based on the maximum tangential stresses that have been reported throughout this chapter. They are restated hereunder (note that the analytical results have been recalibrated using the maximum contact pressure in the final FE-model):

Ply ID [degrees]	1	2	3	4	5	6	7	8	9	10
Analytical	85	256	788	256	85	85	256	788	256	85
Simplified FE	26	198	709	184	30	30	159	639	153	15
Extensive FE	53	174	688	187	45	47	131	638	156	50

TABLE 2.7: Comparison of the maximum tangential stress in each ply for the different models, all stresses are in MPa

As can be seen, the analytical model seems to generally over-estimate the stresses. This is probably because the model has been calibrated using the maximal pressure observed in the FE-model. An alternative would have been to re-calibrate using a weighted mean of the contact pressure, although this being artificial.

The CLT-model is also not correctly representing the decrease in stress towards the outside (compare layer three and eight for example). This effect can be explained by the ignoring of the through-the-thickness variation (cfr. isotropic ring with finite thickness).

The similarity between the two finite elements models is very good. The added value from the second model is that it replaces the quasi-homogeneous stress fields of the first model by stress profiles based on the transmission mechanism. It can also predict the burst pressure based on failure indices.



The extensive finite element model seems to be a good tool to do statements about a ring specimen. However, there remain several open questions. What is the influence of an intrinsic badly known parameter as the friction coefficients? How sensitive are the results to a design parameter as the axial width of the ring? These kind of questions will be the topic of chapter three, in which a sensitivity analysis will be done. It's also the goal to get a broad idea of the influence of the lay-up. In this chapter, a lay-up that was easy to interpret has been used. However, in practice optimization programs are run to design the lay-up and get lay-ups with superior characteristics. Calculations will be made to compare the influence of the lay-up to the friction and the axial width in a rough way.



## Chapter 3

# Sensitivity analysis

In this chapter, the influence of two important variables that are a priori unknown will be investigated: the friction (badly known) and the axial thickness (design parameter). Also, the phenomena that occur in different lay-ups will be demonstrated, by making the ring progressively stiffer in the tangential direction. Both a local and a global sensitivity analysis will be reported to get a comprehensive image of the set-up.

### 3.1 Local sensitivity analysis

A local sensitivity analysis can be done by changing one parameter and looking at the effect on the investigated output variables. Both the stress profiles and the burst pressures will be looked upon.

In Fig. 3.1 the stress profiles in the inner hoop layer are drawn for different values of friction. The investigated values start from a neglectable amount of friction ( $\mu = 0.01$ ) and go up to  $\mu = 0.3$ , a value which is expected to be very high for a contact involving PTFE. Indeed, because of the material choice for the liner (PTFE), the friction can be expected to be rather low. That's why the intervals between the low values of friction are smaller.

In the tangential direction, the profiles are very similar, however they are displaced vertically. There doesn't seem to be a clear (linear) pattern on how high the curves lay depending on the friction. The picture is different in the axial direction: the lower the friction coefficient, the flatter the curves. This effect can be explained easily: if the friction is high, the bending of the liner will 'stretch' the composite more than in the case of low friction. Thus, a non-flat pattern occurs. For low friction coefficients, it is observed that the hill at the edges lays higher than the stress in the middle. They even get higher than where failure is supposed to happen (at the gaps, in the middle of the ring).

### 3.1. Local sensitivity analysis

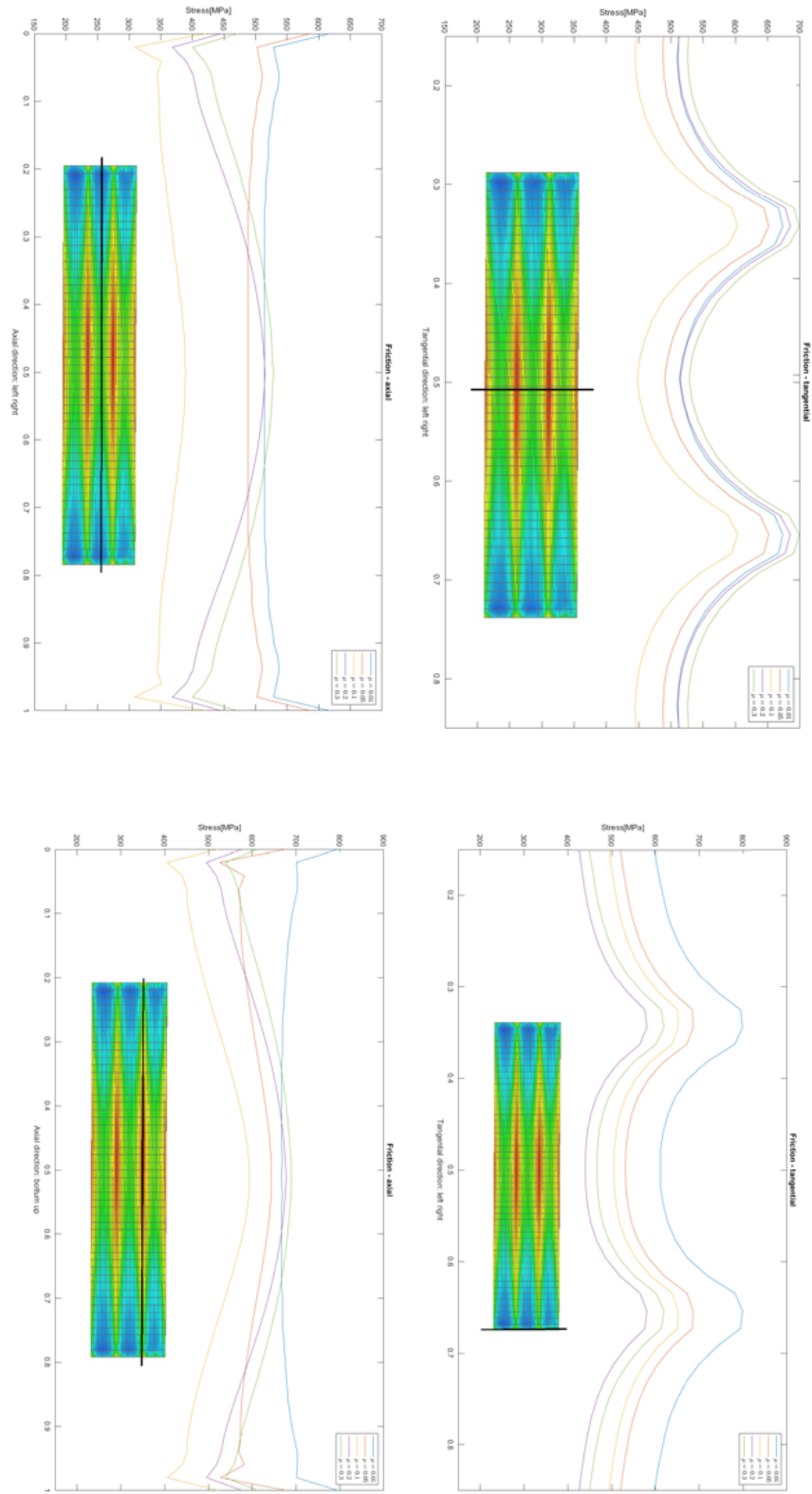


FIGURE 3.1: Stress profiles in the inner hoop layer for different values of friction 40

Nevertheless, a flat pattern does coincide best with the situation in a composite pressure vessel, indicating that there is some 'ideal' situation between  $\mu = 0.05$  and  $\mu = 0.1$ . Indeed, a flat pattern would be obtained while the jump at the edges is at a similar level to the stress in the middle of the ring. This is also the reason why in a real ring test, special measures are taken to minimize the friction (for example lubrication).

The next variable under consideration is the axial width. In Fig. 3.2 the tangential stress profiles in the inner hoop layer are drawn for different axial widths. The investigated range goes from a very thin ring (5 mm) to a ring that is comparable with the liner dimension (100 mm).

In general, it can be observed that the stress levels get higher for thinner rings. In the axial direction, the longer the ring, the higher the stress variation that is observed. This can again be attributed to the bending of the liner around the composite. If the composite is longer, the moment that creates the bending has a higher lever. Because the specimens are quite expensive, it is important to use as little material as possible. Based on this analysis, 25 mm seems to be a good choice, while 5 mm is too thin. Indeed, unwanted high stress levels occur at the edges in this case.

Next, an investigation will happen to develop intuition on how to design a good lay-up. Normally, this design happens based on an optimization problem. This task is well-described in literature and does not fall in the scope of the thesis. However, it remains important to understand the different physical implications of certain choices to assess the quality of the solution of these programs. This understanding will be stimulated by investigating five well-chosen lay-ups:

- $0^\circ/0^\circ/90^\circ/0^\circ/0^\circ/0^\circ/0^\circ/90^\circ/0^\circ/0^\circ$  (lay-up 1)
- $0^\circ/45^\circ/90^\circ/45^\circ/0^\circ/0^\circ/45^\circ/90^\circ/45^\circ/0^\circ$  (lay-up 2)
- $45^\circ/45^\circ/90^\circ/45^\circ/45^\circ/45^\circ/90^\circ/45^\circ/45^\circ$  (lay-up 3)
- $45^\circ/90^\circ/90^\circ/90^\circ/45^\circ/45^\circ/90^\circ/90^\circ/90^\circ/45^\circ$  (lay-up 4)
- $90^\circ/90^\circ/90^\circ/90^\circ/90^\circ/90^\circ/90^\circ/90^\circ/90^\circ/90^\circ$  (lay-up 5)

As can be seen, only two hoop layers are present in lay-up 1. This lay-up is then made stiffer each time in the tangential direction. Lay-up 2 is the one that was used before. Lay-up 5, finally, consist basically of one big orthotropic hoop layer. Note that in lay-up 4 and 5, the third layer is no longer the inner hoop layer, so failure is no longer expected to occur there. However, in first instance the stress profiles are sketched for this layer in Fig. 3.3.

### 3.1. Local sensitivity analysis

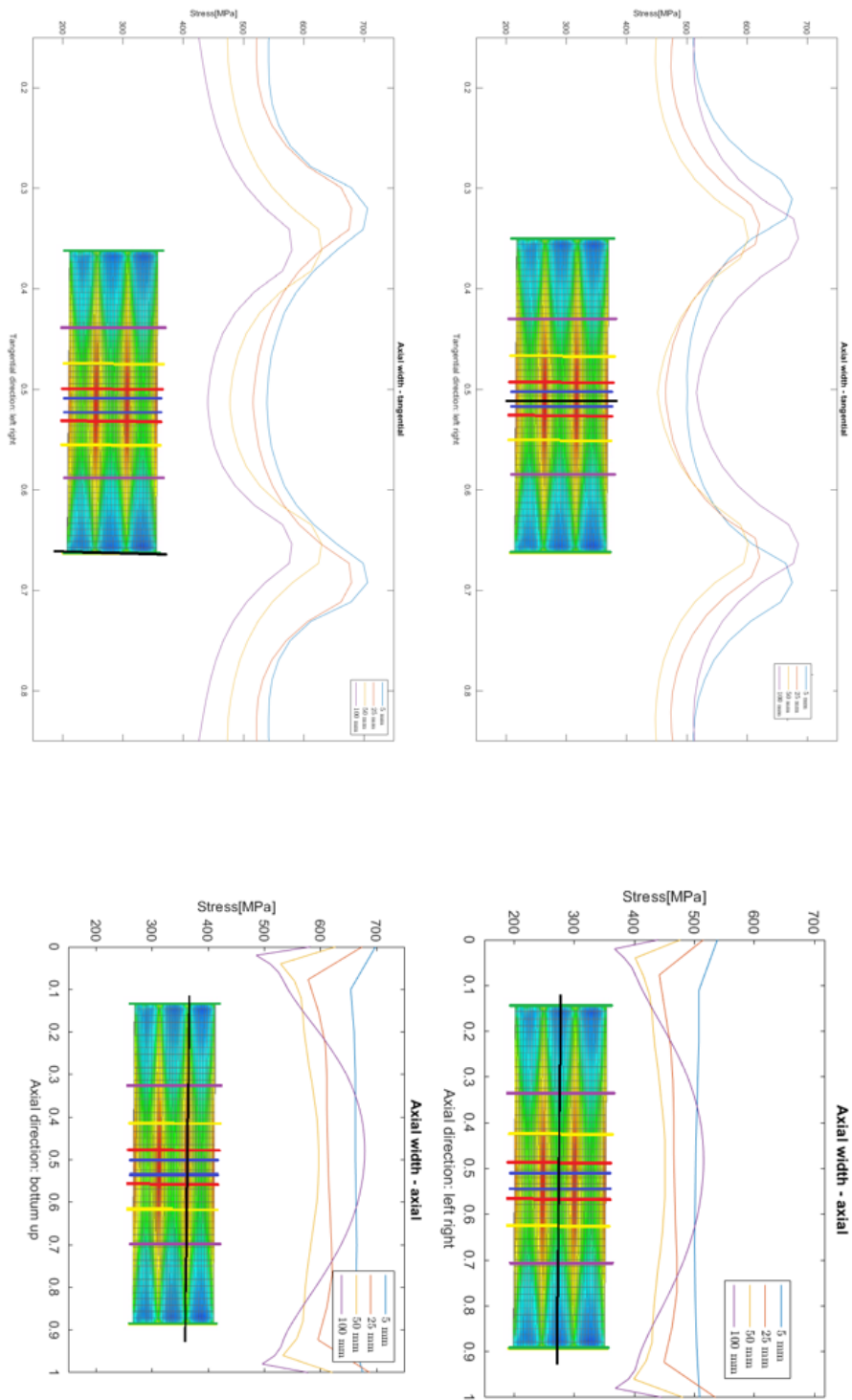


FIGURE 3.2: Stress profiles in the inner hoop layer for different values of axial width

As expected, stress levels get lower for stiffer lay-ups. This is logical since the other plies take a bigger part of the tangential load distribution. It's quite impressive how big the influence of the introduction of an extra hoop layer is. It's also noteworthy that for lay-up 4 and 5, there are no longer stress peaks at the gaps. This is because the layer under consideration is no longer the inner hoop layer, where the stress peaks do still occur.

Next, the first ply failure for the different simulations has been calculated. The predicted burst pressures can be found in Table 3.1.

Friction [°]	0.01	0.05	0.1	0.2	0.3
$p_b$ (bar)	739	459	384	380	237
Width [mm]	5	25	50	100	
$p_b$ (bar)	475	567	503	380	
Lay-up [°]	1	2	3	4	5
$p_b$ (bar)	144	380	711	4524	1923

TABLE 3.1: Burst pressure (bar): results for the different simulations performed during the local sensitivity analysis

Let's first take a look at the results for the friction. Generally, it can be noted that the predicted burst pressure decreases with increasing friction. To understand this, the failure mode should be considered: matrix tension. In this failure index, the in-plane shear stress is present. This stress will logically be higher when there is more friction in the system, increasing the failure index and decreasing the predicted burst pressure.

The ring fails at higher pressures for thinner rings, with the exception of the case of 5 mm. The general pattern can be explained by the fact that the stresses are distributed more evenly for thinner rings (= closer to the actual case in a composite pressure vessel). The ring of 5 mm makes for an exception because the failure no longer occurs in the middle of the ring, but at the edges. This is an unwanted side-effect and should be avoided in practice.

### 3.1. Local sensitivity analysis

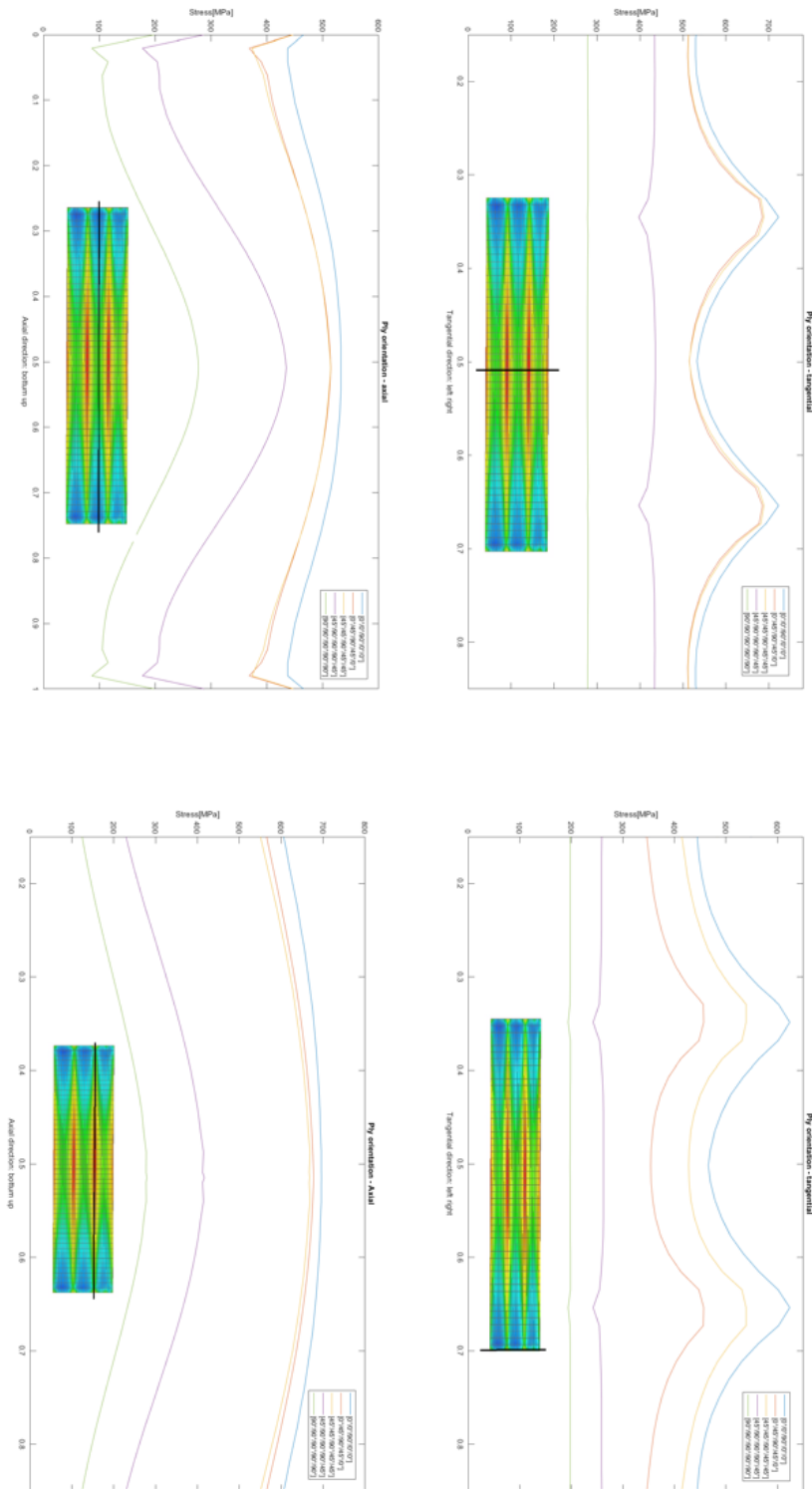


FIGURE 3.3: Stress profiles in layer three for the lay-ups under consideration



The burst pressure increases fast when the lay-up is made stiffer in the tangential direction. The effect is even more drastic when an extra hoop layer is introduced (lay-up 4). It should be noted that the failure then occurs in the newly introduced hoop layer and that the failure mode changes to fibre tension. However, for the big orthotropic layer (lay-up 5) the burst pressure decreases again. What's happening here? First, it should be acknowledged that the failure mode changes again to matrix tension and that it occurs in the inner hoop layer. In this case, the inner hoop layer is in contact with the liner, in contrast to the other lay-ups. This means that the shear stresses will increase heavily which causes early failure. A remark that should be made, is that it is very well possible that in this particular situation the first ply failure does not cause the final breakdown of the structure and that the ring shows itself more resistant than is predicted based on this analysis. This can be investigated with a progressive failure model.

Another important sidemark is the following: based on this analysis, one could conclude that he should just use a very stiff lay-up in the tangential direction. However, it is important to realize that the ring test only duplicates the tangential stresses in a composite pressure vessel. Indeed, in a CPV there are also axial stresses that should be accounted for: these would destroy those particular lay-ups that are too compliant in the axial direction. It is not unreasonable to expect the solution of the optimization problem to be around two times stiffer in the tangential direction than in the axial direction (since the stresses are approximately doubled). Also, the drastic influence of the hoop layers shows that most orientations will be close to 0 degrees or 90 degrees (and not close to 45 degrees). Off course, these rules of thumbs should be interpreted in the loose sense.

To get a more clear idea on the orders of magnitude of the influence of the different parameters, a tornado-diagram can be found in Fig. 3.4. Important to note is that the width of the bars is logarithmically scaled. Not surprisingly, the orientation is heavily dominant. Nevertheless, the variation for the friction and the width is also certainly non-neglectable. This shows the importance of a good control mechanism for the friction and a well-thought choice for the axial width.

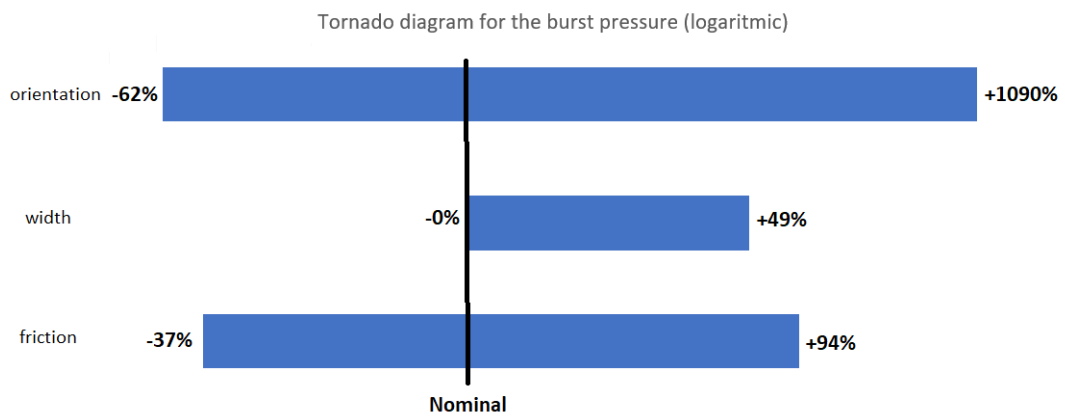


FIGURE 3.4: Tornado diagram for the burst pressure: influence of the different parameters. The width of the bars is logarithmically scaled

## 3.2 Global sensitivity analysis

Now that the one-dimensional sensitivity analysis is done, a global sensitivity analysis can give an even more complete image of the system. In a global sensitivity analysis, the different inputs are changed interactively to check their influence on the output. It's common sense that this kind of problem is inherently computationally demanding. Therefore, a big amount of methods has been developed to limit the computational cost of the investigation. In this subsection, the systematic of (26) has been used. It involves the calculation of the Sobol'-indices and the determination of a histogram of the burst pressure.

These so-called Sobol' indices are a way to objectify the importance of different input variables that help explain an output variable. Let's consider a model  $Y = M(X)$  which defines the output variable  $Y$  as a function of the set of input variables  $X$

$$Y = M_0 + \sum_{i=1}^n M_i(X_i) + \sum_{i < j \leq n} M_{ij}(X_i, X_j) + \dots + \sum_{1 \dots m} M_{ij}(X_i, \dots, X_n)$$

The variation in  $Y$  can then be seen as a sum of the variances of the individual model parts

$$Var(Y) = \sum_u Var(M_u(X_u))$$

The Sobol'-indices are then expressed as

$$S_{\mathbf{u}} = \frac{Var(M_u(X_u))}{Var(y)} \text{ with } \sum S_i = 1$$

Hereafter, an efficient algorithm will be used to estimate the indices. The starting point of this method are a number of well-chosen experiments, as will be explained in the next subsection.

### 3.2.1 Determination of the Sobol' indices

A first step was to generate a relatively large number of samples. All of the setpoints that were discussed in the previous subsection are being combined, good for a total of  $N = 5 * 5 * 4 = 100$  simulations. Taking into account that each simulation took quite some time, this was a time-consuming part of the project. Especially since the software did not allow to fully automate the work. Nonetheless, the results can be found in Appendix 5.2, where the predicted burst pressures are given in bar.

Based on these results, a polynomial chaos expansion (PCE) of the burst pressure can be determined. This is basically a polynomial model fit that expresses the output variable in function of the input (stochastic) variables. Since there is little a priori knowledge about the input variables, Laplace criterion states that uniform distributions should be employed. In this case, it can be proven that the so-called Legendre-polynomials show optimal performance. The first four Legendre polynomials can be found in Table 3.2. It can be shown that they are orthonormal (27).

$n$	$P_n(x)$	normalization factor
0	1	$\sqrt{\frac{1}{2}}$
1	$x$	$\sqrt{\frac{3}{2}}$
2	$\frac{3x^2-1}{2}$	$\sqrt{\frac{5}{2}}$
3	$\frac{5x^3-3x}{2}$	$\sqrt{\frac{7}{2}}$
4	$\frac{35x^4-30x^2+3}{8}$	$\sqrt{\frac{9}{2}}$

TABLE 3.2: Normalized Legendre polynomials, up to order four (27)

Before developing the model, the explanatory variables have to be chosen. Based on the 1D-analysis, the choice fell on the axial width ( $h$ ), the friction ( $\mu$ ), the mean ply orientation ( $\bar{x}$ ) and the percentage of hoop layers ( $\bar{h}$ ). Note that those last two variables are an artificial and somehow incomplete way to represent the lay-up, limiting the number of variables to represent it to only two. Since there are four input variables in our investigation, a logical extension of the polynomials up to order  $n$  is given by

$$P_n(h, \mu, \bar{x}, \bar{h}) = \sum_{i=0}^n \sum_{j=0}^{n-i} \sum_{k=0}^{n-i-j} \sum_{l=0}^{n-i-j-k} P_i(h) P_j(\mu) P_k(\bar{x}) P_l(\bar{h}) = \sum_{i=0}^n \sum_{j=0}^{n-i} \sum_{k=0}^{n-i-j} \sum_{l=0}^{n-i-j-k} f_{ijkl}$$

Using the stars-and-bars method from combinatorial mathematics (28), it is relatively easy to show that such a summation contains the following number of terms

$$\sum_{i=0}^n \frac{(n+3)!}{n!3!}$$

There are several ways to determine an 'optimal' polynomial, but here the standard LLS-method was chosen. If there are  $i$  samples and  $c$  coefficients, the matrix system is given by

$$\begin{bmatrix} f_{1,1} & \cdot & \cdot & \cdot & f_{c,1} \\ \cdot & \cdot & & & \cdot \\ \cdot & & \cdot & & \cdot \\ \cdot & & & \cdot & \cdot \\ f_{1,i} & \cdot & \cdot & \cdot & f_{c,i} \end{bmatrix} \begin{bmatrix} C_1 \\ \cdot \\ \cdot \\ \cdot \\ C_c \end{bmatrix} = \begin{bmatrix} p_1 \\ \cdot \\ \cdot \\ \cdot \\ p_i \end{bmatrix}$$

where  $f_{j,i}$  is the value of base function  $j$  for sample  $i$ ;  $C_i$  are the coefficients that have to be determined and  $p_i$  is the observed pressure for sample  $i$ .

This system of equations has been coded in Matlab, using the *syms* package. An example of the code for  $n = 2$  is shown below.

```
% n=2 r^2=0.756
terms=15;
syms fr wi me ho c000 c100 c010 c001 c0001 c110 c101 c011 c1001 c0101 c0011...
      c200 c020 c002 c0002
f(fr,wi,me,ho,c000,c100,c010,c0001,c001,c110,c101,c011,c1001,c0101,c0011,...
  c200,c020,c002,c0002)= c000+c100*fr+c010*wi+c001*me+c0001*ho+...
  c110*fr*wi+c101*fr*me+c011*wi*me+c1001*fr*ho+c0101*wi*ho+...
  c0011*me*ho+c200*0.5*(3*fr^2-1)+c020*0.5*(3*wi^2-1)+...
  c002*0.5*(3*me^2-1)+c0002*0.5*(3*ho^2-1);
data=importdata("matrix_calculation.xlsx");
l=size(data);l=l(1);
A=zeros(l,1);
b=zeros(l,1);
for i=1:l
    for j=1:terms
        C_row=zeros(1,terms);
        C_row(j)=1;
        A(i,j)=subs(f,[fr wi me ho c000 c100 c010 c001 c0001 c110 c101...
            c011 c1001 c0101 c0011 c200 c020 c002 c0002], ...
            [data(i,1) data(i,2) data(i,3) data(i,4) C_row(1) C_row(2) ...
            C_row(3) C_row(4) C_row(5) C_row(6) C_row(7) C_row(8) C_row(9)...
            C_row(10) C_row(11) C_row(12) C_row(13) C_row(14) C_row(15)]);
    end
    b(i,1)=data(i,5);
end
C=A\b;
```

Afterwards, the  $R^2$  and the adjusted  $R^2$  value are calculated to determine how much of the variation is explained by the model and to check for model inflation. Again, an example of the code for  $n = 2$  is shown below.

```
M=zeros(1,1);
sum=0;
for i=1:l
    M(i,1)=subs(f,[fr wi me ho c000 c100 c010 c001 c0001 c110 c101 c011 ...
        c1001 c0101 c0011 c200 c020 c002 c0002], [data(i,1) data(i,2)...
        data(i,3) data(i,4) C(1) C(2) C(3) C(4) C(5) C(6) C(7) C(8) C(9)...
        C(10) C(11) C(12) C(13) C(14) C(15)]);
    sum=sum+1/1*(data(i,5)-M(i,1))^2;
end
va=var(data(:,5));
r_squared=1-sum/va;
```

This calculation has been performed for different polynomials up to  $n = 4$  (for  $n = 5$  there would have been more coefficients than samples). The  $R^2$  and the adjusted  $R^2$  values can be found in Fig. 3.5. Based on this graph, the choice has been made to go on with the solution for  $n = 4$ , since the  $R^2$  value was the highest ( $= 0.9787$ ) and the adjusted  $R^2$  kept increasing significantly.

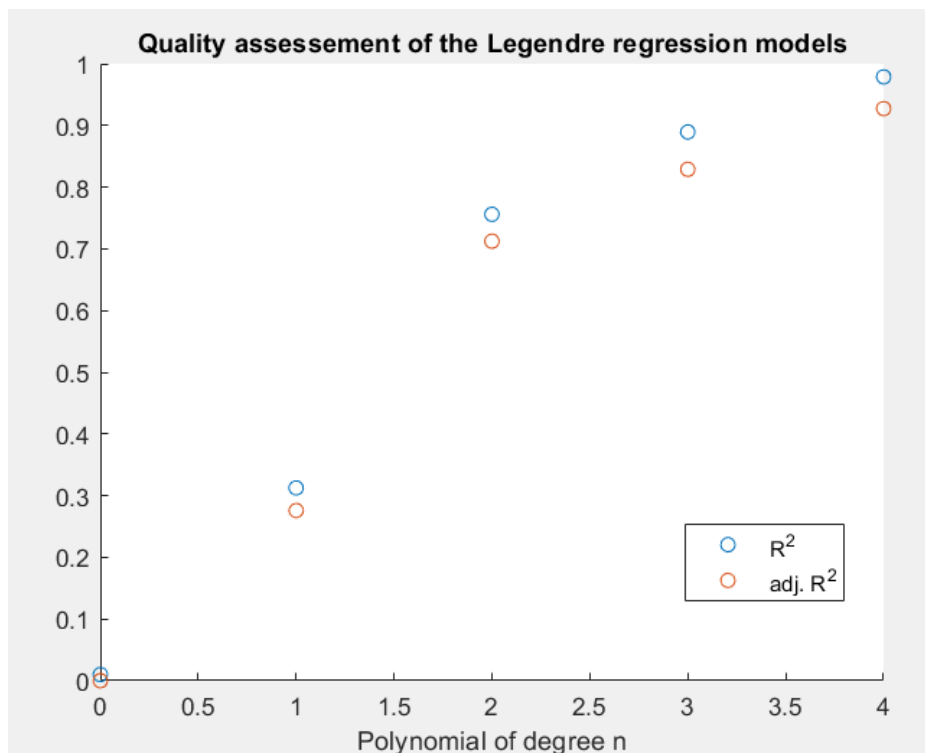


FIGURE 3.5:  $R^2$  and the adjusted  $R^2$  for  $n$  up to four.

Based on this solution, a global sensitivity analysis can happen at a low computational cost. Indeed, sampling can happen cheaply by making use of the polynomial fit. But let's first focus on the Sobol-indices: it can be shown that, due to the specific choice of the used functions, they are directly related to the calculated coefficients (26):

$$S_{\mathbf{u}} = \frac{\sum_{i \in \mathbf{u}} c_i^2}{\sum_{i=1}^n c_i^2}$$

where  $\mathbf{u}$  refers to a subset of input variables and  $c_i$  are the coefficients of the expansion, belonging to an expression that is a function of several inputs ( $i \in \mathbf{u}$ ). Using this formula, the indices have been calculated. They can be seen in Table 3.3. A more graphical interpretation can be found in Fig. 3.6.

Variable(s)	Sobol-index
$\bar{h}$	0.46
$\bar{x}$	0.29
$\mu$	0.1
h	0.06
Interactions	0.09

TABLE 3.3: Sobol indices based on the polynomial chaos expansion

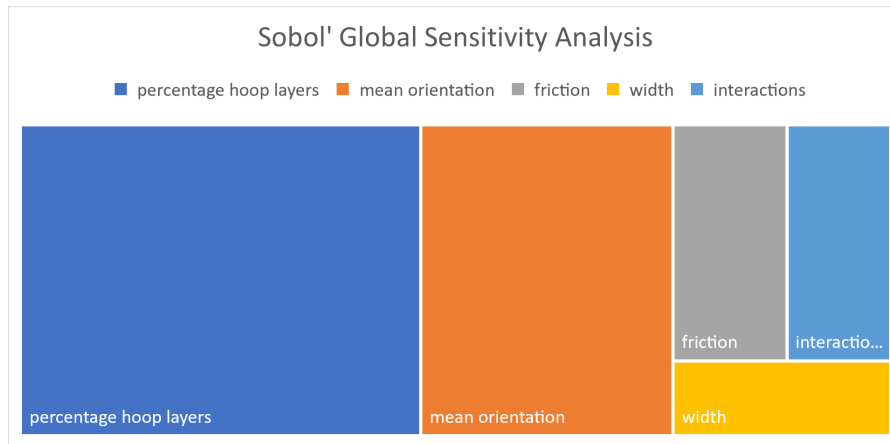


FIGURE 3.6: Decomposition of the variance of the output by use of Sobol indices.

The interpretation of the Sobol-indices is the following: 46 percent of the output variance is caused by the variance in the percentage of hoop layers, 29 percent by the variance in the mean ply orientation, 10 percent by the variation in the friction, 6 percent due to the variation in the axial width and 9 percent due to interactions between the different variables. This is in line with the expectations based on the local sensitivity analysis.

### 3.2.2 Histogram of the burst pressure

The PCE also enables to do a very cheap 'Monte Carlo'-like simulation to visualize the behavior of the burst pressure. The choice has been made to do a separate analysis for the different lay-ups that were examined before. This facilitates the interpretation and makes it easier to visualize everything. The code that was used to simulate lay-up 1 can be found below.

```
% Monte Carlo
% lay-up 1
D=zeros(1000,1);
fri=zeros(1000,1);
wid=zeros(1000,1);
for i=1:1000
    fri(i)=0.01+(0.3-0.01)*rand();
    wid(i)=5+(100-5)*rand();
    D(i,1)=subs(f,[fr wi me ho c000 c100 c010 c001 c0001 c110 c101 c011 ...
    c1001 c0101 c0011 c200 c020 c002 c0002 c111 c1101 c0111 c1011 c120 ...
    c210 c012 c021 c102 c201 c1002 c2001 c0102 c0201 c0012 c0021 c300...
    c030 c003 c0003 c400 c040 c004 c0004 c2002 c0022 c0202 c1102 c1012 ...
    c0112 c2101 c1201 c0121 c0211 c1021 c2011 c220 c022 c202 c211 c121...
    c112 c301 c031 c103 c013 c310 c130 c1003 c0103 c0013 c3001 c0301...
    c0031 c1111], ...
        [fri(i) wid(i) 18 0.2 C(1) C(2) C(3) C(4) ...
        C(5) C(6) C(7) C(8) C(9) C(10) C(11) C(12) C(13) C(14) ...
        C(15) C(16) C(17) C(18) C(19) C(20) C(21) C(22) C(23) ...
        C(24) C(25) C(26) C(27) C(28) C(29) C(30) C(31) C(32) C(33)...
        C(34) C(35) C(36) C(37) C(38) C(39) C(40) C(41) C(42) C(43)...
        C(44) C(45) C(46) C(47) C(48) C(49) C(50) C(51) C(52) C(53) ...
        C(54) C(55) C(56) C(57) C(58) C(59) C(60) C(61) C(62) C(63)...
        C(64) C(65) C(66) C(67) C(68) C(69) C(70)]);
end
histogram(D,25)
```

In this way, each of the five lay-ups has been simulated 1000 times. The mean, median, deviation and coefficient of variation  $\sigma/\mu$  have been reported in Table 3.4. A histogram of the burst pressure can be found in Fig. 3.7. To get a more consistent view of the spread, the graphs have been normalized  $(X - \mu)/\sigma$  in Fig. 3.8.



Some conclusions can be drawn. The coefficient of variation does not seem to vary much for the different lay-ups. All the distributions seem quite similar. They have a long but weak left tail, while the right tail is much more populated. This is good news since the strength of the left tail will strongly affect the determination of the safety factor. Indeed, a weak and short tail means that the safety factor will be lower than in the case of a long and highly populated tail. Further, there do not seem to be much new patterns in the generated data.

Lay-up/Core measure	Mean	Median	Deviation	Coefficient of variation
1	458	419	127	0.28
2	503	535	170	0.34
3	1130	830	350	0.31
4	6420	7498	1400	0.22
5	2936	2659	700	0.24

TABLE 3.4: Key statistics for the lay-ups investigated in the Monte Carlo simulation. All pressures are in bar.

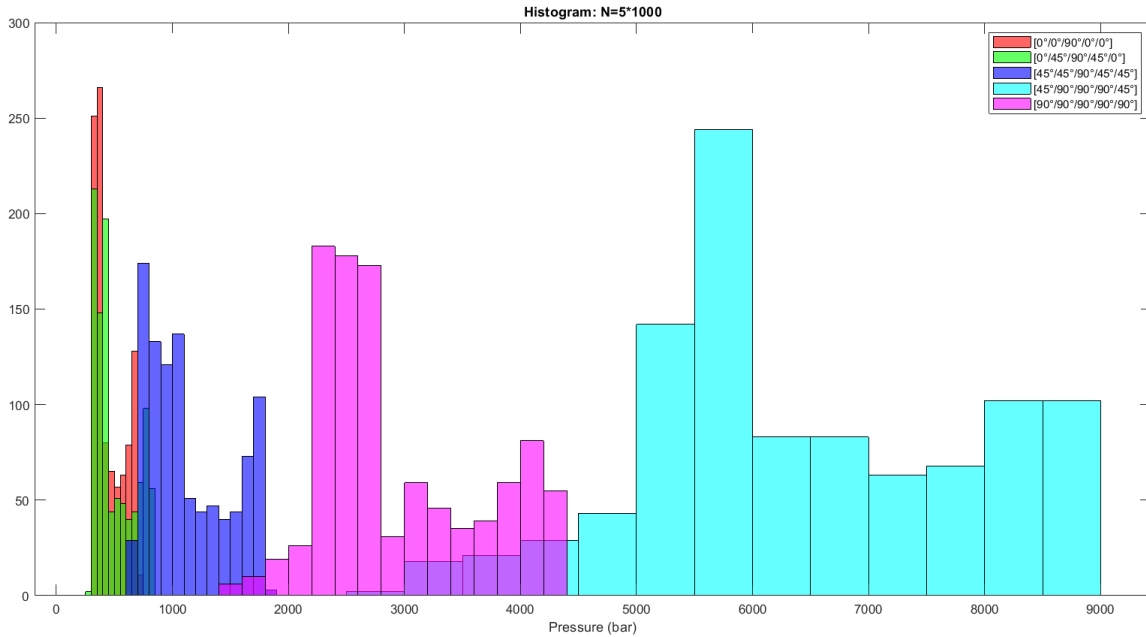


FIGURE 3.7: Histogram of the Monte Carlo simulation.

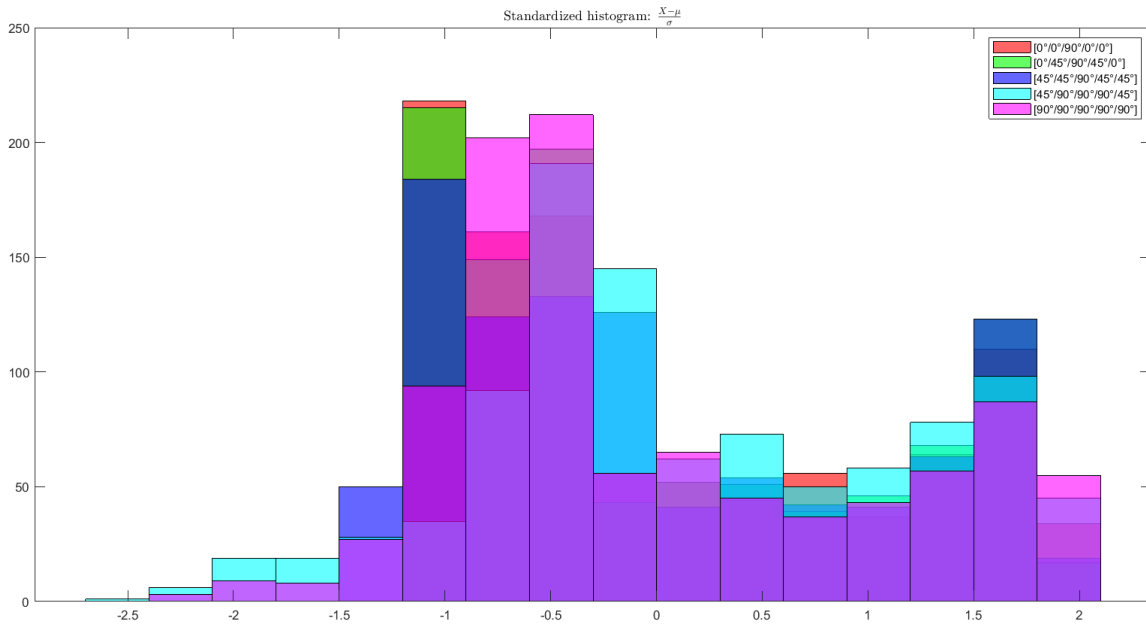


FIGURE 3.8: Standardized histogram of the Monte Carlo simulation.

### 3.3 Conclusions

In this chapter, a sensitivity analysis was performed to the ring test. The behaviour of the stress profiles was explained for a number of different widths, frictions and lay-ups in the local analysis. It was shown that the width can't be chosen randomly and that a friction monitoring system is necessary. It is advised to use a ring of a bit less than 25 mm (5 mm is certainly too narrow); standard measures to decrease the friction should be implemented, although there is no need for extreme low friction. Besides this, the solution of a numerical lay-up optimization program was predicted: the tangential stiffness will be around twice times the axial stiffness and most layers will be either close to 0 degrees or close to 90 degrees.

In the global analysis, a polynomial chaos expansion was determined and the interactions between the different variables were examined. In combination with a Monte Carlo simulation, it was shown that the expected distributions of the burst pressure have a long, but weak left tail. This is good news, since it will decrease the safety factor. The coefficient of variation was similar for the different lay-ups. This is also good news, since it increases the predictive power of the ring test.



## Chapter 4

# Conclusions

In this thesis, an elaborate overview was given of the use of a ring test to determine the burst pressure of a composite pressure vessel. The advantage of a ring test is clear: one can use less material and thus save money. However, it was shown that there are also disadvantages: the stress profiles are certainly not flat within a ply like in a composite pressure vessel, and there is a rather strong sensitivity to the friction and the axial width. These effects should be taken into account when the safety factor is determined and might limit the decrease in that safety factor that was envisioned. Like mostly in engineering, there is a trade-off between the full-scaled test set-up and the ring test. It is up to the individual engineer or company to make a choice, based on the complete information that is provided in this thesis and in other sources. This choice will depend on the phase in the development cycle and the scale of the future production. Early in the development cycle and for small amounts of products, the ring test seems to have a competitive advantage. If one is planning to sell very big amounts of the same product, it might pay off to do a full-scaled experiment campaign.

### 4.1 Results

In the introductory chapter 1, a narrowing approach was followed. Starting from the usage case for fibre composites, things got more specific. The use of composite pressure vessels in fuel cell electric vehicles was explained. Structural problems then appeared and the potential of a ring test was introduced to tackle them. The work plan of the text was explained.

In chapter 2 different models were developed:

- An analytical model of a hydraulic pressure applied onto a cylindrical vessel was coded to get an idea of the orders of magnitude of the stresses and the distribution along the plies.
- A first finite element model was developed. It modelled a hydraulic pressure at the inside of a composite ring. It served again as a control mechanism and enabled to see the differences with a finite element model of the ring test.
- Finally, in the third model the whole ring test was drawn up. It included contact mechanisms and plastic behaviour of the PTFE liner.
- This model was validated based on physical insight, a comparison with the other models and a convergence analysis.
- Pressure and stress profiles in the inner hoop layer were reported.
- This model could also be used to predict the burst pressure, under the assumption that the first ply failure would lead to the final breakdown of the structure.

In chapter 3 an extensive sensitivity analysis was performed:

- In the local sensitivity analysis, stress profiles were shown for different frictions, axial widths and lay-ups. The burst pressure appeared to be a rather sensitive variable, emphasizing the importance of well-thought usage of the ring test.
- It was shown that the stress profiles for the ring around 25 mm (= axial width) were closest to the situation in a composite pressure vessel. If they were larger, undue bending occurred. If they were smaller, unwanted edge effects occurred.
- It was shown that the friction should be made reasonably low. If the friction is too high, undue stretching of the laminate occurs.
- The solution of a numerical optimization program to determine the lay-up was predicted. The tangential stiffness will be around twice times the axial stiffness. Most layers will be close to either 0 degrees or 90 degrees.
- In the global sensitivity analysis, the interaction between the variables was modelled. By combining a polynomial chaos expansion with a Monte Carlo analysis, it could be shown that the left tail was long, but weak. This is good news since it implies a limitation of the safety factor.
- It was also clear that the coefficient of variation for different lay-ups was comparable. Again being good news, since it increases the predictive value of the ring test to assess burst pressure.

## 4.2 Further work

As is often the case, the answer to certain questions leads to new, interesting issues that should also be tackled. The following improvements and further work are suggested:

- Implement a progressive failure program to assess whether first ply failure leads to breakdown of the mechanism. This is often the case, but since matrix tension failure occurred a lot, it remains unsure. Indeed, the matrix material is rather tough, while the fibre is brittle.
- In this thesis, intuitive lay-ups were used. If one is really going to test an optimized structure, this specific structure should be implemented in the finite element model. Then, a comparison should be made between 'theory' and experiment. This can be done quick, since the adaptations necessary are modest.
- Investigate the influence of manufacturing imperfections, such as fibre misalignment, fibre strength variation, layer thickness variation, ... This cannot be done in a classical finite element program since most of these variables are local and should be treated as random fields.
- Based on the previous points, a safety factor can be calculated. The determination of this variable will greatly determine the potential of the ring test. It is expected to be lower than the safety factor of 2.25 that is used nowadays.



# Chapter 5

## Appendices

### 5.1 Code for CLT-calculations (Van Bavel)

```
%% Define parameters
...

%% Loading
N_ax    = pressure*radius/2;
N_hoop  = pressure*radius;
loading = [N_hoop/2;
          N_hoop;
          0;
          0;
          0;
          0];

%% Calculate laminate stresses

% Calculate principal stiffness matrices
C = zeros(3,3,number_of_plyes);
for i = 1:number_of_plyes
    if material(i) == "liner"
        C(:, :, i) = [E1L/(1-nu12L*nu21L)      nu12L*E2L/(1-nu12L*nu21L)    0;
                     nu21L*E1L/(1-nu12L*nu21L)  E2L/(1-nu12L*nu21L)      0;
                     0                          0                          G12L];
    elseif material(i) == "composite"
        C(:, :, i) = [E1/(1-nu12*nu21)      nu12*E2/(1-nu12*nu21)    0;
                     nu12*E1/(1-nu12*nu21)  E2/(1-nu12*nu21)      0;
                     0                          0                          G12];
    end
end
end
```



---

```

% Transform principal matrix for other ply-orientations
for i = 1:number_of_plies
    t=ply_angle(i);
    T = [cos(t)^2    sin(t)^2    2*sin(t)*cos(t) ;
         sin(t)^2    cos(t)^2    -2*sin(t)*cos(t);
         -sin(t)*cos(t)    sin(t)*cos(t)    cos(t)^2-sin(t)^2];
    R = [1 0 0;
         0 1 0;
         0 0 2];
    T_R = R*T/R;
    C(:, :, i) = inv(T)*C(:, :, i)*T_R;
end

% Calculate ABD matrices
A = zeros(3,3);
B = zeros(3,3);
D = zeros(3,3);
for i = 1:number_of_plies
    z_top    = -total_thickness/2 + sum(thickness(1:i)); %z-axis pointing to bottom
    z_bottom = -total_thickness/2 + sum(thickness(1:i-1));

    A = A + C(:, :, i)*thickness(i);
    B = B + 0.5*C(:, :, i)*(z_top^2 - z_bottom^2);
    D = D + (1/3)*C(:, :, i)*(z_top^3 - z_bottom^3);
end
stiffness_matrix = [A B; B D];

% Calculate strains of the laminate
%strains = stiffness_matrix \ (stress*total_thickness) due to symmetry
%conditions, strains calculated from A-matrix only since there can be no
%curvatures in a cylindrical PV. This is otherwise not taken into account
strains = A \ loading(1:3);

```

---

```

% Calculate ply stresses
ply_stress_principal = zeros(3, number_of_plyes);
for i = 1:number_of_plyes
    z_top      = -total_thickness/2 + sum(thickness(1:i)); %z-axis pointing to bottom
    z_bottom   = -total_thickness/2 + sum(thickness(1:i-1));
    z_mean     = (z_top + z_bottom)/2;

    ply_strains = strains(1:3);% + z_mean*strains(4:6)
    % do not add because curvatures are zero due to symmetry conditions in cylinder
    ply_stress = C(:, :, i)*(ply_strains);
    t=ply_angle(i);
    T = [cos(t)^2    sin(t)^2    2*sin(t)*cos(t) ;
         sin(t)^2    cos(t)^2    -2*sin(t)*cos(t);
         -sin(t)*cos(t)    sin(t)*cos(t)    cos(t)^2-sin(t)^2];

    ply_stress_principal(:, i) = T*ply_stress;
end

```

## 5.2 Results of the test campaign

5 mm						25 mm					
Fr./PlV	1	2	3	4	5	Fr./PlV	1	2	3	4	5
0.01	506	676	878	1534	854	0.01	761	691	2849	9021	4754
0.05	487	704	846	1789	801	0.05	682	723	2612	10743	4533
0.1	441	576	814	1731	849	0.1	592	646	2390	10363	4756
0.2	414	475	642	1521	948	0.2	471	567	1491	8789	4580
0.3	401	541	789	1489	989	0.3	411	548	1814	8129	4897
<b>50 mm</b>						<b>100 mm</b>					
Fr./PlV	1	2	3	4	5	Fr./PlV	1	2	3	4	5
0.01	656	306	480	9387	3047	0.01	391	739	1019	4760	1800
0.05	502	326	539	9401	4784	0.05	231	459	580	7537	2270
0.1	384	387	691	9338	5085	0.1	304	284	551	7224	2228
0.2	335	503	1040	9142	4684	0.2	144	380	711	4524	1923
0.3	424	528	1130	7458	4208	0.3	382	237	711	4333	1626

FIGURE 5.1: Predicted burst pressures for various setpoints, in bar.



# Bibliography

- [1] Sandy Thomas (2009) Fuel Cell and Battery Electric Vehicles Compared. Sub-section 2.1
- [2] M. Kuhn, N. Himmel, M. Maier (2000) Design and analysis of full composite pressure vessels. Page 65, Table 1.
- [3] Justin Hale (2006) Boeing 787 from the Ground Up, qtr04 06, a quarterly publication (boeing.com/commercial/aeromagazine). Page 18.
- [4] Fabio Malgioglio (2020) Material variability across the scales in unidirectional composites Virtual material characterisation under longitudinal tension. Selection of Table 1.1, page 5.
- [5] BMW (25-04-2022) How hydrogen fuel cell cars work (<https://www.bmw.com/en/innovation/how-hydrogen-fuel-cell-cars-work.html>).
- [6] Sandy Thomas (2009) Fuel Cell and Battery Electric Vehicles Compared. Sub-section 3.
- [7] P. Nimdum, B. Patamaprohm, J. Renard, S. Villalonga (2015) Experimental method and numerical simulation demonstrate non-linear axial behaviour in composite filament wound pressure vessel due to thermal expansion effect. Figure 1, page 2.
- [8] Maxime Bertin, Damien Halm, B. Magneville, Jacques Renard, Philippe Sare, Stephane Villalonga (2015) One year OSIRHYS IV project synthesis: mechanical behaviour of 700 bar type iv high pressure vessel code qualification. Section 1.
- [9] Woe Tae Kim, Seong Su Kim (2020) Design of a segment-type ring burst test device to evaluate the pressure resistance performance of composite pressure vessels. Paper on the use of a ring test.
- [10] Fabio Malgioglio (2020) Material variability across the scales in unidirectional composites Virtual material characterisation under longitudinal tension. Figure 5.10, page 135.
- [11] P. Mallick (2007) Fiber-Reinforced Composites: Materials, Manufacturing, and Design. Section 5,5.

- 
- [12] P. Mallick (2007) Fiber-Reinforced Composites: Materials, Manufacturing, and Design. Figure 5.24, page 427
- [13] Maxime Bertin, Damien Halm, B. Magneville, Jacques Renard, Philippe Saffr´e, St´ephane Villalonga (2012) One year OSIRHYS IV project synthesis: mechanical behaviour of 700 bar type iv high pressure vessel code qualification. Figure 3.b on page 3; introductory subsection.
- [14] Garvin Tam (2004) Coefficients of Friction for Teflon, <https://hypertextbook.com/facts/2004/GarvinTam.shtml> (09-05-2022).
- [15] Woe Tae Kim, Seong Su Kim (2020) Design of a segment-type ring burst test device to evaluate the pressure resistance performance of composite pressure vessels. Figure 2 on page 3.
- [16] Woe Tae Kim, Seong Su Kim (2019) Evaluation of mechanical properties of composite pressure vessels using a segment-type ring burst test device. Subsection 3,2.
- [17] Mohammad Halawa and Naser Al-Huniti (2019) Optimum Design of Carbon/Epoxy Composite Pressure Vessels Including Moisture Effects. Subsection 2,1.
- [18] Bill Webster (2021), <https://www.fidelisfea.com/post/first-order-vs-second-order-elements-in-fea> (26-04-2022)
- [19] L.C.S. Nunes, F.W.R. Dias, H.S. da Costa Mattos (2011) Mechanical behavior of polytetrafluoroethylene in tensile loading under different strain rates. Fig. 4 on page 793.
- [20] Woe Tae Kim, Seong Su Kim (2020) Design of a segment-type ring burst test device to evaluate the pressure resistance performance of composite pressure vessels. Table 1 and 2, page 3.
- [21] Woe Tae Kim, Seong Su Kim (2020) Design of a segment-type ring burst test device to evaluate the pressure. Figure 10 on page 6.
- [22] B. Gentilleau, S. Villalonga, F. Nony, H. Galiano (2014) A probabilistic damage behavior law for composite material dedicated to composite pressure vessel. Figure 6 on page 4.
- [23] P.F. Liu, L.J. Xing, J.Y. Zheng (2013) Failure analysis of carbon fiber/epoxy composite cylindrical laminates using explicit finite element method. Table 3, page 55.
- [24] Yosuke Ueki, Hans Lilholt, Bo Madsen (2020) Experimental evaluation of stiffness predictions of multiaxial flax fibre composites by classical laminate theory. Figure 10, page 14.

- [25] Robert Jones (1999) *Mechanics of Composites*. Figure 6-17.
- [26] Michel Tosin, Adriano Côrtes, Americo Cunha Jr (2020) *A Tutorial on Sobol' Global Sensitivity Analysis Applied to Biological Models*. Chapter 1.
- [27] Eric W. Weisstein (1999) <https://archive.lib.msu.edu/crcmath/math/math/1/1175.htm> (26/04/2022)
- [28] Mei Li, Jubayer Nirjhor, Sandeep Bhardwaj, <https://brilliant.org/wiki/integer-equations-star-and-bars/> (26/04/2022)